Monthly Notices of the ROYAL ASTRONOMICAL SOCIETY

MNRAS **516,** 2736–2756 (2022) https://doi.org/10.1093/mnras/stac2262
Advance Access publication 2022 August 13

Dwarf AGNs from Optical Variability for the Origins of Seeds (DAVOS): insights from the dark energy survey deep fields

Colin J. Burke [1,2★] Xin Liu,[1,3] Yue Shen,[1,3] Kedar A. Phadke,[1] Qian Yang,[1] Will G. Hartley,[4] Ian Harrison [5] Antonella Palmese [6,7] Hengxiao Guo [1,3,8] Kaiwen Zhang,[9] Richard Kron [6,10] David J. Turner [11] Paul A. Giles [11] Christopher Lidman [12] Yu-Ching Chen [1] Robert A. Gruendl,[1,2] Ami Choi,[13] Alexandra Amon,[14] Erin Sheldon,[15] M. Aguena [16] S. Allam,[6] F. Andrade-Oliveira,[16,17] D. Bacon [18] E. Bertin [19,20] D. Brooks,[21] A. Carnero Rosell [16] M. Carrasco Kind [1,2] J. Carretero [22] C. Conselice,[5,23] M. Costanzi,[24,25,26] L. N. da Costa,[16,27] M. E. S. Pereira,[28,29] T. M. Davis [30] J. De Vicente [31] S. Desai,[32] H. T. Diehl,[6] S. Everett,[33] I. Ferrero [34] B. Flaugher,[6] J. García-Bellido [35] E. Gaztanaga [36,37] D. Gruen,[38] J. Gschwend,[16,27] G. Gutierrez,[6] S. R. Hinton [30] D. L. Hollowood [33] K. Honscheid,[13,39] B. Hoyle [38] D. J. James,[40] K. Kuehn,[41,42] M. A. G. Maia,[16,27] J. L. Marshall,[43] F. Menanteau,[1,2] R. Miquel,[22,44] R. Morgan,[45] F. Paz-Chinchón,[2,46] A. Pieres [16,27] A. A. Plazas Malagón [47] K. Reil,[48] A. K. Romer,[11] E. Sanchez,[31] M. Schubnell,[28] S. Serrano,[36,37] I. Sevilla-Noarbe,[31] M. Smith [49] E. Suchyta [50] G. Tarle,[28] D. Thomas [18] C. To [48,51,52] T. N. Varga,[53,54] and R.D. Wilkinson[11] (DES Collaboration)

Affiliations are listed at the end of the paper

Accepted 2022 August 5. Received 2022 July 8; in original form 2021 November 5

ABSTRACT

We present a sample of 706, $z < 1.5$ active galactic nuclei (AGNs) selected from optical photometric variability in three of the Dark Energy Survey (DES) deep fields (E2, C3, and X3) over an area of 4.64 deg^2. We construct light curves using difference imaging aperture photometry for resolved sources and non-difference imaging PSF photometry for unresolved sources, respectively, and characterize the variability significance. Our DES light curves have a mean cadence of 7 d, a 6-yr baseline, and a single-epoch imaging depth of up to $g \sim 24.5$. Using spectral energy distribution (SED) fitting, we find 26 out of total 706 variable galaxies are consistent with dwarf galaxies with a reliable stellar mass estimate ($M_* < 10^{9.5}$ M$_\odot$; median photometric redshift of 0.9). We were able to constrain rapid characteristic variability time-scales ($\sim$ weeks) using the DES light curves in 15 dwarf AGN candidates (a subset of our variable AGN candidates) at a median photometric redshift of 0.4. This rapid variability is consistent with their low black hole (BH) masses. We confirm the low-mass AGN nature of one source with a high S/N optical spectrum. We publish our catalogue, optical light curves, and supplementary data, such as X-ray properties and optical spectra, when available. We measure a variable AGN fraction versus stellar mass and compare to results from a forward model. This work demonstrates the feasibility of optical variability to identify AGNs with lower BH masses in deep fields, which may be more 'pristine' analogues of supermassive BH seeds.

Key words: black hole physics – galaxies: active – galaxies: dwarf.

1 INTRODUCTION

Virtually every massive galaxy contains a supermassive black hole (SMBH) in its centre (Kormendy & Richstone 1995). There is growing evidence for the existence of intermediate-mass BHs (IMBHs, $M_\bullet = 10^2 \sim 10^6$ M$_\odot$; Greene, Strader & Ho 2020) in dwarf galaxies beyond the handful of well-studied examples: NGC 4395 (Filippenko & Ho 2003), Pox 52 (Barth et al. 2004), Henize 2-10 (Reines & Volonteri 2015), and RGG 118 (Baldassare et al. 2015). The recent discovery of the gravitational-wave transient GW190521 with a merger remnant mass of 142^{+28}_{-16} M$_\odot$ (LIGO Scientific Collaboration & Virgo Collaboration 2020) provides the strongest evidence for IMBHs. However, the occupation fraction of black holes (BHs) in the dwarf galaxy regime remains poorly constrained (Greene et al. 2020).

SMBHs as massive as several billion solar masses were already formed when the universe was only a few hundred Myr old (e.g. Fan et al. 2001; Wu et al. 2015; Bañados et al. 2018; Wang et al. 2021). How they were able to form so quickly is an outstanding question in cosmology (Volonteri 2010; Inayoshi, Visbal & Haiman 2020). At least three channels have been proposed for the formation

★ E-mail: colinjb2@illinois.edu

of the seeds of SMBHs: Pop. III stellar remnants (e.g. Madau & Rees 2001), direct collapse (e.g. Haehnelt & Rees 1993; Bromm & Loeb 2003; Begelman, Volonteri & Rees 2006), or star cluster evolution (e.g. Gürkan, Freitag & Rasio 2004; Portegies Zwart et al. 2004). The occupation fraction of BHs in local dwarf galaxies (i.e. $M_* < 10^{10}\,M_\odot$; Greene et al. 2020) and their mass functions traces the SMBH seeding mechanism at high redshifts (e.g. Greene 2012; Reines & Comastri 2016). The occupation function of BHs in ultradwarf ($M_* = 10^5 \sim 10^6\,M_\odot$) galaxies is important for understanding the origin of some LIGO binary BHs (Palmese & Conselice 2021). However, systematic approaches to finding such dwarf active galactic nuclei (AGNs) have only recently begun.

For example, deep X-ray surveys can be used to identify low-mass and low-luminosity AGNs at low and intermediate redshifts (Civano et al. 2012; Fiore et al. 2012; Young et al. 2012; Luo et al. 2017; Xue 2017). However, these surveys are expensive and often plagued by contamination from X-ray binaries. Radio searches have also identified low-mass AGNs in star-forming dwarf galaxies (Mezcua, Suh & Civano 2019; Reines et al. 2020), although they are subject to the low detection rate of radio cores of AGNs. Alternatively, optical colour selection is much less expensive but is biased against smaller BHs and/or lower Eddington ratios. Optical emission line selection, such as with BPT diagram diagnostics (Baldwin, Phillips & Terlevich 1981; Veilleux & Osterbrock 1987), is known to miss AGNs with line ratios dominated by star formation (Baldassare et al. 2016; Agostino & Salim 2019), particularly in low-metallicity (Groves, Heckman & Kauffmann 2006) and low-mass galaxies without sufficient spectral resolution (Trump et al. 2015), and because of the dilution from star-forming regions within the spectral aperture in low-mass galaxies (Yan & Blanton 2012; Mezcua & Domínguez Sánchez 2020). Furthermore, the standard optical narrow emission line diagnostics used to identify AGNs may fail when the BH mass falls below $\sim 10^4\,M_\odot$ for highly accreting IMBHs and for radiatively inefficient IMBHs with active star formation, because the enhanced high-energy emission from IMBHs could result in a more extended partially ionized zone compared with models for SMBHs, producing a net decrease in the predicted [O III]/Hβ and [N II]/Hα emission line ratios (Cann et al. 2019). Recently, dwarf AGNs have been identified using coronal line emission signatures (Cann et al. 2021; Molina et al. 2021), but this requires high-quality infrared (IR) spectra.

Compared to other techniques, variability searches should be more sensitive to AGNs with lower Eddington ratios given the anticorrelation between Eddington ratio and optical variability (MacLeod et al. 2010; Rumbaugh et al. 2018). The optical variability-selection technique for unobscured AGNs and quasars is well-established (Trevese et al. 2008; Butler & Bloom 2011; Cartier et al. 2015; De Cicco et al. 2015; Kumar et al. 2015; Tie et al. 2017; Sánchez-Sáez et al. 2018; De Cicco et al. 2019; Pouliasis et al. 2019; Della Costa, Sarajedini & Strolger 2020; Kimura et al. 2020; Poulain et al. 2020). Also see Elmer et al. (2020) and Secrest & Satyapal (2020) for recent studies based on n ear-IR and mid-IR (MIR) variabilities. Variability results in an incomplete selection, missing optically obscured AGNs or those with bright host galaxies that dilute the variability from the accretion disc. The selection rates are expected to depend on the sensitivity/photometric precision of the survey and the exact selection criteria used (Burke et al. 2022). However, using variability as a complementary AGN selection technique to identify dwarf AGNs is a relatively new technique (Baldassare, Geha & Greene 2018; Baldassare, Geha & Greene 2020; Guo et al. 2020; Martínez-Palomera et al. 2020; Ward et al. 2021a)

In this work, we perform a systematic search for variable AGN using Dark Energy Survey (DES; Dark Energy Survey Collaboration 2016) deep field imaging (Hartley et al. 2022). We choose the DES deep fields because of the exceptional depth ($g \sim 24.6$), ~7 d cadence with a total baseline of ~6 yr, and availability of multiwavelength imaging and spectroscopy. Using these data, we are able to identify optically variable AGN candidates in dwarf galaxies to $z \sim 1.5$ for the first time.

This paper is organized as follows. In Section 2, we describe the DES observations, our methods for constructing light curves, and our variability-selection procedure, in Section 3, we present our catalogue of variability-selected dwarf AGNs and study our AGN detection fraction, in Section 4, we compare our results to previous works, in Section 5, we summarize our new findings and conclude.

2 OBSERVATIONS AND DATA ANALYSIS

2.1 The Dark Energy Survey

The DES (2013–2019 January) was a wide-area ~5000 deg^2 survey of the southern galactic cap in the *grizY* bands. It used the Dark Energy Camera (Flaugher et al. 2015; Bernstein et al. 2017) with a 2.2-degree diameter field of view mounted at the prime focus of the Victor M. Blanco 4-m telescope on Cerro Tololo in Chile. The data quality varies due to seeing and weather variations. The DES absolute photometric calibration has been tied to the spectrophotometric Hubble CALSPEC standard star C26202 and has been placed on the AB system (Oke & Gunn 1983). In addition to the wide-area survey, the DES contains a 27 deg^2 multiepoch survey to search for Type Ia supernovae (SNe) called DES-SN (Kessler et al. 2015). DES-SN is composed of 10 DES fields each with a uniform cadence of about 7 d in the *griz* bands during the observing season. DES-SN operated during the 'science verification' – year 5 (SV–Y5) seasons (six-year total baseline).

2.2 The Dark Energy Survey dep fields

In this work, we restrict our analysis to three of the 11 (composed of 10 DES-SN fields plus the COSMOS field) DES deep fields (SN-E2, SN-C3, SN-X3) with weekly cadence from the DES-SN program (Kessler et al. 2015) and with 8-band (*ugrizJHK$_S$*) deblended, stacked model-based photometry from Hartley et al. (2022) (Table 1). These fields overlap with the European Large Area *ISO* Survey (Oliver et al. 2000), the *Chandra* Deep Field-South (Luo et al. 2017), and *XMM* Large Scale Structure survey fields (Garcet et al. 2007), respectively. Supplementary DECam *u*-band imaging was obtained in these fields. Additional *JHK$_S$* imaging data are from the VIDEO (overlaps with SN-E2, SN-C3, and SN-X3; Jarvis et al. 2013) and UltraVISTA (overlaps with COSMOS; McCracken et al. 2012) surveys, and the final deblended catalogue is built to a uniform depth of $i = 25$. The total area of the fields with NI R overlap is 4.64 deg^2 after masking bright stars and artefacts. We will leverage the deep 8-band colour information for star–galaxy separation and stellar mass estimates.

2.3 Star–galaxy separation

Star–galaxy separation is performed using a supervised machine-learning classifier trained on DES-COSMOS *ugriz* and UltraVISTA survey *JHK$_S$* band imaging using the *Hubble Space Telescope (HST)* morphological star–galaxy classifications of Leauthaud et al. (2007) as the ground truth. The trained classifier is then applied to the DES-SN fields, with additional validation shown in Hartley et al. (2022). A *k*-nearest neighbours method is used, which yields a purity and completeness of ~ 99 per cent or better (Hartley et al. 2022). A

Table 1. Summary of DES deep fields used in this work. The SN-E3 field is referred to as a 'shallow' field by Kessler et al. (2015) but the coadd photometry from Hartley et al. (2022) is built to the same depth as the 'deep' fields, SN-C3 and SN-X3. Column 4 refers to the single-epoch limiting PSF magnitude depth where the detection efficiency has fallen to 50 per cent (Kessler et al. 2015). The median number of epochs refers to our light curves after requiring $N_{\rm epoch} > 100$.

Field	RA [deg (hh:mm:ss)]	Dec. [deg (hh:mm:ss)]	Limiting g mag	Median $N_{\rm epochs}$
SN-C3	52.6484 (03:30:35.6)	−28.1000 (−28:06:00.0)	24.5	364
SN-E2	9.5000 (00:38:00.0)	−43.9980 (−43:59:52.8)	23.5	120
SN-X3	36.4500 (02:25:48.0)	−4.6000 (−04:36:00.0)	24.5	163

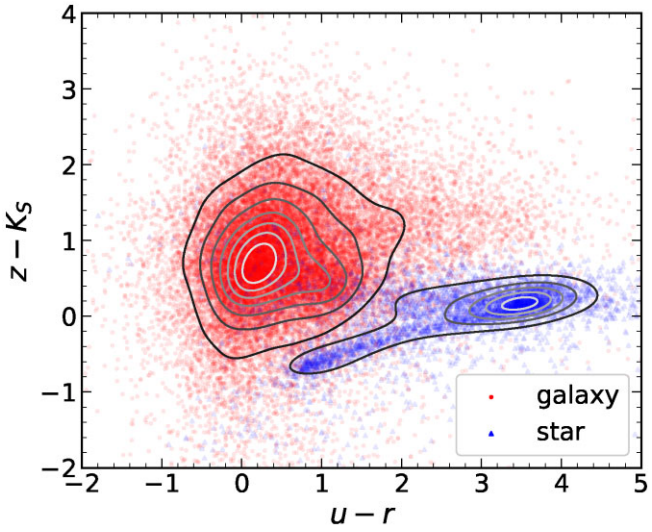

Figure 1. Colour–colour plot demonstrating the star–galaxy classifier using the machine-learning method described in Section 2.3. For clarity, a subset of all objects in SN-C3 is plotted under density contours.

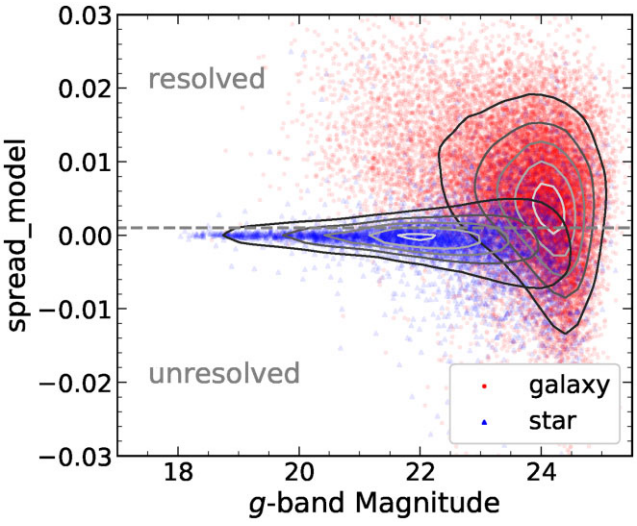

Figure 2. Spread model versus median g-band PSF magnitude for galaxies (red circles) and stars (blue triangles) classified using the machine learning classifier described in Section 2.3. The dashed grey line shows the cut at `spread_model` =0.001 between resolved and unresolved sources. For clarity, a subset of the total data points in SN-C3 is plotted under density contours.

colour–colour plot demonstrating the star–galaxy classifier is shown in Fig. 1.

2.4 Light-curve construction

We construct light curves using g-band point spread function (PSF) magnitudes for unresolved sources. For resolved sources, we use aperture-based difference imaging analysis (DIA) magnitudes. While light curves in other bands can be useful, it is computationally expensive to re-compute difference images in all bands. Given AGNs generally are more variable in bluer bands and DES-SN did not perform u-band imaging, we chose to restrict our variability selection to the g band. In addition, the accretion disc SED is expected to shift into the bluer/UV part of the spectrum at lower BH masses (e.g. Cann et al. 2019). Furthermore, differences between variability timescales between bands are small, scaling like $\lambda^{0.17}$ (MacLeod et al. 2010; Suberlak, Ivezić & MacLeod 2021). To determine whether to use PSF or DIA photometry, we use the `spread_model` estimator to separate resolved and unresolved sources (e.g. Desai et al. 2012; Soumagnac et al. 2015). This estimator is the normalized simplified linear discriminant between a local PSF model $\tilde{\phi}$ and an extended model $\tilde{G}$:

$$\texttt{spread\_model} = \frac{\tilde{G}^T W p}{\tilde{\phi}^T W p} - \frac{\tilde{G}^T W \tilde{\phi}}{\tilde{\phi}^T W \tilde{\phi}}, \quad (1)$$

where $\tilde{G}$ is the local PSF model convolved with a circular exponential disc model with scale-length 1/16th of the full width at half-maximum of the PSF model, p is the image vector centred on the source, and W is a weight matrix constant along the diagonal. We chose the threshold `spread_model` =0.001 (i.e. use DIA magnitudes if `spread_model` >0.001, otherwise use PSF magnitudes). We use the median `spread_model` of all measurements for each source to select a pure sample of resolved sources. The threshold is shown in Fig. 2. As a demonstration of our DIA photometry, we also show example PSF and DIA light curves of a resolved galaxy in Fig. 3 and for an unresolved non-variable star in Fig. 4. DIA allows us to measure variability from the central AGN (a point source) after subtracting the flux from the non-variable extended host galaxy. Simple aperture photometry is generally inadequate for resolved sources, because seeing variations can contaminate the aperture with varying fractions of light from the host galaxy.

Our difference imaging pipeline is similar to the DES-SN pipeline of Kessler et al. (2015), used to identify Type Ia SNe and other transients in the DES-SN fields. However, we need to re-compute the difference images across all observing seasons with a single template image to achieve a consistent zero-point light curve. In contrast, the DES-SN difference images were computed using a different template in each season. The DIA pipeline uses the HOTPANTS code (Becker 2017), which follows the algorithm described in Alard & Lupton (1998) and Alard (2000). We build a PSF kernel across each single-epoch science image and convolve the template to match the PSF in

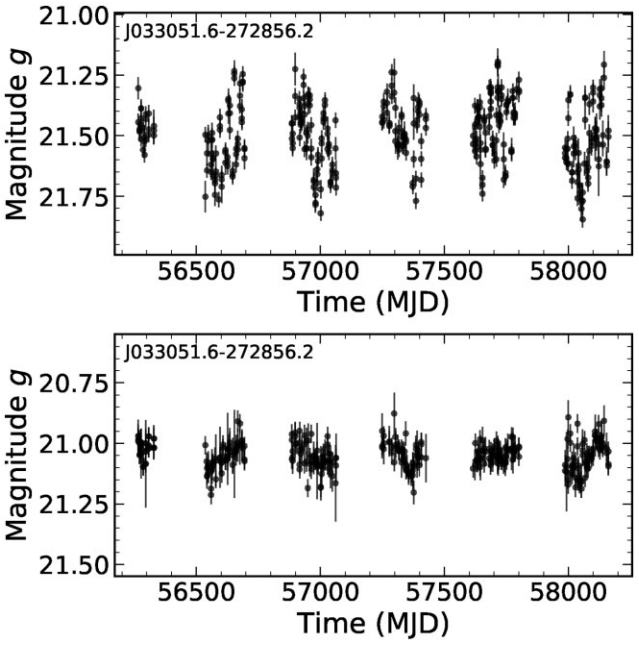

Figure 3. Example PSF (top panel) and DIA (bottom panel) light curves of a resolved variable galaxy. The PSF light curve includes additional false variability due to seeing variations. Significant intrinsic variability is still detected in this source using DIA photometry. The slight difference in magnitude for resolved sources is due to the larger area enclosed in the DIA aperture.

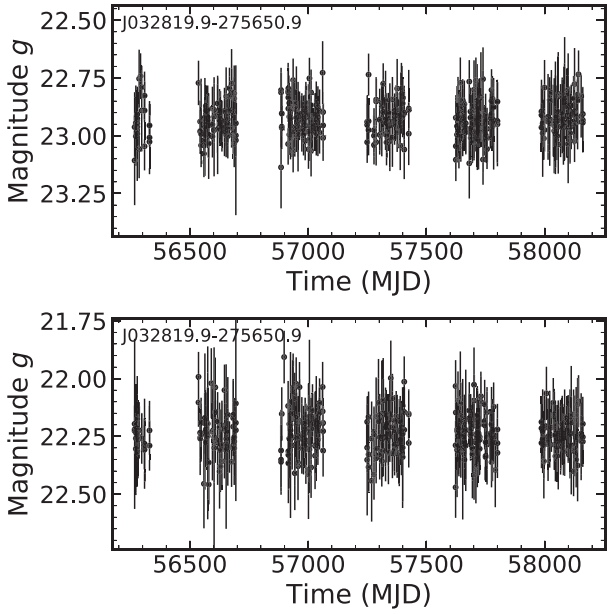

Figure 4. Example PSF (top panel) and DIA (bottom panel) light curves of an unresolved non-variable star. The slight difference in magnitude is due to the larger area enclosed in the DIA aperture.

the science image. HOTPANTS works by minimizing the equation

$$-2\log L = \sum_i \left([T \otimes K](x_i, y_i) - I(x_i, y_i)\right)^2, \quad (2)$$

where T is the template frame, K is the PSF kernel, I is the science frame, and $\otimes$ denotes convolution. We assume that the kernel K can be decomposed into Gaussian basis functions which are allowed to vary on differing spatial orders. This takes the form,

$$K(u, v) = \sum_n a_n K_n(u, v), \quad (3)$$

where $K_n(u, v) = e^{-(u^2+v^2)/2\sigma_k^2} u^i v^j$ and $n = (i, j, k)$. The spatial order is confined to the size of kernel.

We adapted the pipeline from Kessler et al. (2015) to produce a single template used for all DES-SN seasons (to achieve a constant zero-point), and perform forced photometry centred on detections in the template image. We follow the criteria of Kessler et al. (2015) for creating the template image, selecting Y3 images with sky noise $\sigma_{\rm sky} < 2.5\,\sigma_{\rm sky,\,min}$. After this, we use up to 10 images with the smallest PSF. The template and image subtraction are done on a per-CCD basis (2048 × 4096 pixels). We use SWarp to create the template coadds and reproject each science image to the template WCS. We use SExtractor (Bertin & Arnouts 1996) in double image mode to perform forced photometry on the template and difference image. We use a 5σ threshold for detection in the template image. We use a circular aperture of 5 arcsec in diameter to be larger than the seeing disc. This restriction to nuclear variability precludes us from detecting off-nuclear (recoiling or wandering) SMBHs (Blecha et al. 2016; Reines et al. 2020; Ward et al. 2021b) $\gtrsim$ 2.5 arcsec from a galaxy's centroid. Although it is possible to measure the position of the variability using the difference frames, image artifects caused by small astrometric misalignments makes this difficult in practice. Therefore, we leave detecting off-nuclear AGNs to future studies.

2.5 Variability-selection procedure

2.5.1 Variability significance

After constructing light curves and determining whether to use PSF or DIA magnitudes, we perform outlier rejection on each light curve using a sliding window approach. We use a window size of 150 d and a 3σ rejection threshold where $\sigma = 1.4826$ MAD, where MAD is the median absolute deviation. We also empirically correct the photometric uncertainties for systematics following the method of Sesar et al. (2007), as detailed in Appendix A. We use the χ^2-based maximum-likelihood estimator from Shen et al. (2019) to estimate the intrinsic variability of sources, as described below.

For a light curve with photometry X_i and measurement error σ_i and unknown excess variance σ_0^2 from intrinsic variability, we have

$$\mathrm{Var}[X_i] = \sigma_0^2 + \sigma_i^2 = \frac{\sigma_0^2}{g_i}, \quad (4)$$

where

$$g_i \equiv \frac{\sigma_0^2}{\sigma_0^2 + \sigma_i^2} = \frac{1}{1 + (\sigma_i/\sigma_0)^2} \quad (5)$$

quantifies the 'goodness' of X_i for measuring σ_0^2. g_i varies from 0 for points with $\sigma_i \gg \sigma_0$ to 1 for points with $\sigma_i \ll \sigma_0$. The sum of g_i over all data points then provides a goodness of measuring the intrinsic variability using the time-series and approaches the total number of data points in the limit of $\sigma_i \ll \sigma_0$.

The likelihood function given X_i and a constant flux model of $\mu = <X_i>$ with both measurement errors and intrinsic variance is

$$-2\log L = \sum_{i=1}^{N} \frac{(X_i - \mu)^2}{\sigma_0^2 + \sigma_i^2} + \sum_{i=1}^{N} \log\left(\sigma_0^2 + \sigma_i^2\right). \quad (6)$$

Minimizing the likelihood function, we obtain an estimate of σ_0 as

$$\hat{\sigma}_0^2 = \frac{\sum (X_i - \mu)^2 g_i^2}{\sum g_i},$$
$$\mathrm{Var}[\sigma_0^2] = \frac{\hat{\sigma}_0^4}{\sum g_i \frac{\sum (X_i-\mu)^2 g_i^3}{\sum (X_i-\mu)^2 g_i^2} - \sum g_i^2/2}. \quad (7)$$

To estimate the value of μ, we use the optimal weights of the photometry based on σ_i and σ_0:

$$\hat{\mu} = \frac{\sum \frac{X_i}{\sigma_0^2+\sigma_i^2}}{\sum \frac{1}{\sigma_0^2+\sigma_i^2}} = \frac{\sum X_i g_i}{\sum g_i}, \ \mathrm{Var}[\mu] = \frac{\sigma_0^2}{\sum g_i}. \quad (8)$$

Equations (7) and (8) are solved iteratively. We have neglected the (usually small) covariance between $\hat{\mu}$ and $\hat{\sigma}_0^2$. We define signal-to-noise ratio estimator as

$$\mathrm{SNR} = \frac{\hat{\sigma}_0}{\mathrm{RMS}[\sigma_0]}. \quad (9)$$

As noted by Shen et al. (2019), SNR saturates near $\sqrt{2(N_{\mathrm{epoch}}-1)}$, where N_{epoch} is the number of epochs in the light curve. To classify a source as variable, we require $N_{\mathrm{epoch}} > 100$ and SNR > 3. We will compare this estimator with other variability statistics later to justify the adopted threshold.

2.5.2 Transient Rejection

To reject flaring transients from our sample (e.g. SNe, tidal disruption events, microlensing events) with time-scales of less than ∼1 yr, we determine if the variability is confined to only one light-curve season. For each of the six seasons, N_i in the light curve, we compute the SNR using the light-curve data in the other five seasons without the data from season N_i. If any of these seasonal SNR values falls below 2, we flag the light curve as a possible transient and exclude it from our analysis. Examples of flagged light curves are shown in Fig. 5. Still, rare long-duration optical stellar transients, such as outbursts of massive stars, can mimic AGN variability (Burke et al. 2020). Therefore, we must be cautious before confirming the AGN nature of our candidates.

2.5.3 AGN-like variability

To further increase the purity of our sample, we use the autocorrelation information of the light curves to reject light curves with spurious variability which appear as white noise. This contrasts to AGN light curves which show a correlated behaviour, commonly modelled as a damped random walk (DRW; MacLeod et al. 2010; Kelly, Sobolewska & Siemiginowska 2011). Specifically, we use the Ljung–Box test under the null hypothesis that the light-curve data are independently distributed with time (Ljung & Box 1978). The Ljung–Box test is a portmanteau test, which does not evaluate the light curve against a particular model of intrinsic variability. We convert the test statistic to a significance that the light curve is 'AGN-like' without any particular priors on the structure function or model assumptions. We denote this quantity as σ_{LB}. Finally, we note that σ_{LB} will be small for AGNs that vary predominately on time-scales less than the ∼7 d DES-SN cadence. We discuss this in more detail and the possible selection biases this may induce below.

2.5.4 Comparison to a quasar–selection method

As described above, our non-parametric SNR and σ_{LB} criteria do not evaluate the light curve against a particular model of intrinsic variability. This is necessary to avoid selection biases associated with particular model parameters. In contrast, the Butler & Bloom (2011) method is based on two criteria: a χ^2-test variability estimator (σ_{var}) and a model significance (σ_{QSO}) evaluated against a parameterization of the ensemble quasar structure function as a function of apparent magnitude using quasars in SDSS Stripe 82. It is unclear if this parameterization is optimal for the selection of dwarf AGNs, because the structure function of dwarf AGNs is not well studied. In addition, the fractional contamination of the host galaxy flux is generally larger for dwarf AGNs, which have lower AGN luminosities than quasars. This means the parameterization as a function of apparent magnitude may not be valid for the sources we are interested in. However, Baldassare et al. (2018, 2020) found 0.25–1.0 per cent of $z < 0.15$ dwarf galaxies had a detectable variable AGN, depending on the light-curve baseline, using the Butler & Bloom (2011) method.

To better study the efficacy of both techniques, we compare our variability estimator to the Butler & Bloom (2011) selection method as implemented in the QSO_FIT code.[1] The comparison is shown in Fig. 6. After removing transient sources, we find that our SNR metric is well correlated with σ_{var} for variable sources (SNR > 3). In addition, we find that σ_{LB} and σ_{QSO} are well correlated for variable sources (SNR > 3). This may imply that the AGNs in our sample have close-enough structure functions to normal quasars given the sensitivity of the Butler & Bloom (2011) σ_{QSO} test. Nevertheless, this comparison validates our variability-selection procedure, which has fewer assumptions about the intrinsic properties of AGN variability.

2.6 Photometric redshifts

We use the method of Yang et al. (2017), which is trained on both non-AGN galaxies and AGNs, to determine the photometric redshifts z_{ph} of our sources using the available optical/NIR photometry from Hartley et al. (2022). We start with sources classified as galaxies from the DES deep field k-nearest neighbours classifier (as opposed to stars). Then, we use the template-fitting method described in Yang et al. (2017) to further classify sources as galaxies or quasars. Because we are looking for variable dwarf (low luminosity) AGNs, we consider both quasar and galaxy classes. After determining the classification, we obtain z_{ph} values for each source using the asymmetries in the relative flux distributions as a function of redshift and magnitude (Yang et al. 2017), where source fluxes were measured from the coadded photometry. The procedure is identical for both variable and non-variable galaxies/quasars, because we are interested in measuring the variable fraction as a function of stellar mass. Throughout this work, we adopt these z_{ph} values for our sources for the stellar mass estimation and analysis, described below.

2.7 Stellar mass estimation

We use the CIGALE code (Burgarella, Buat & Iglesias-Páramo 2005; Noll et al. 2009; Boquien et al. 2019) to estimate the stellar masses by fitting the broad-band spectral energy distribution (SED) composed of deblended stacked, model-based *ugrizJHK*$_S$ photometry. We performed SED fitting with both resolved and unresolved sources. CIGALE works by imposing a self-consistent energy balance

[1] http://butler.lab.asu.edu/qso_selection/index.html

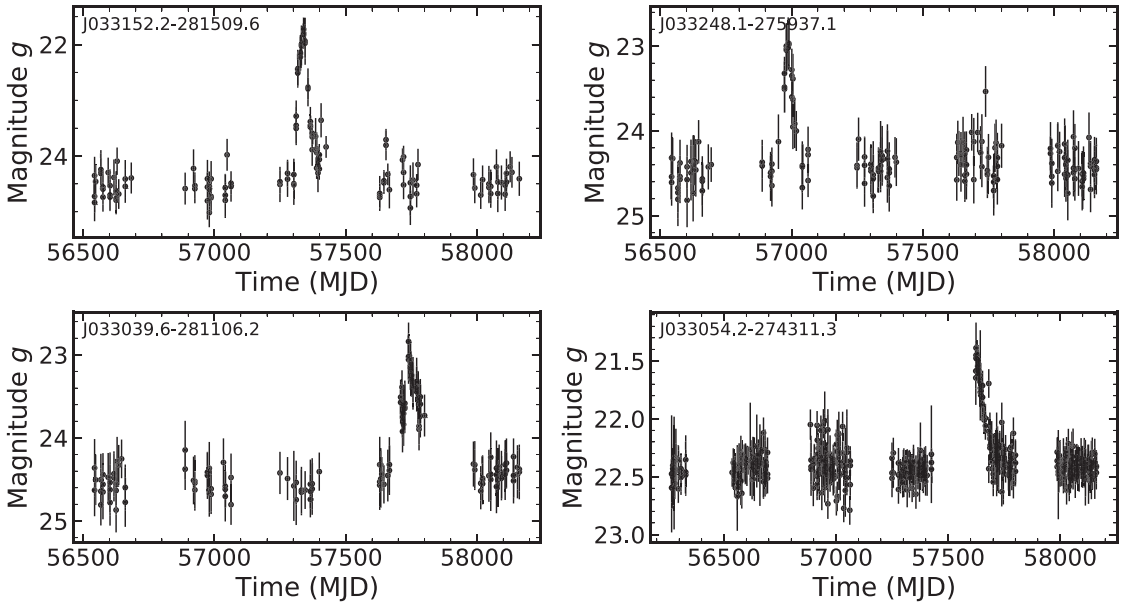

Figure 5. Examples of clear non-AGN-like transients rejected by our method described in Section 2.5.2, including DES J033152.2-281509.6 (known superluminous SN DES15C3hav; Angus et al. 2019).

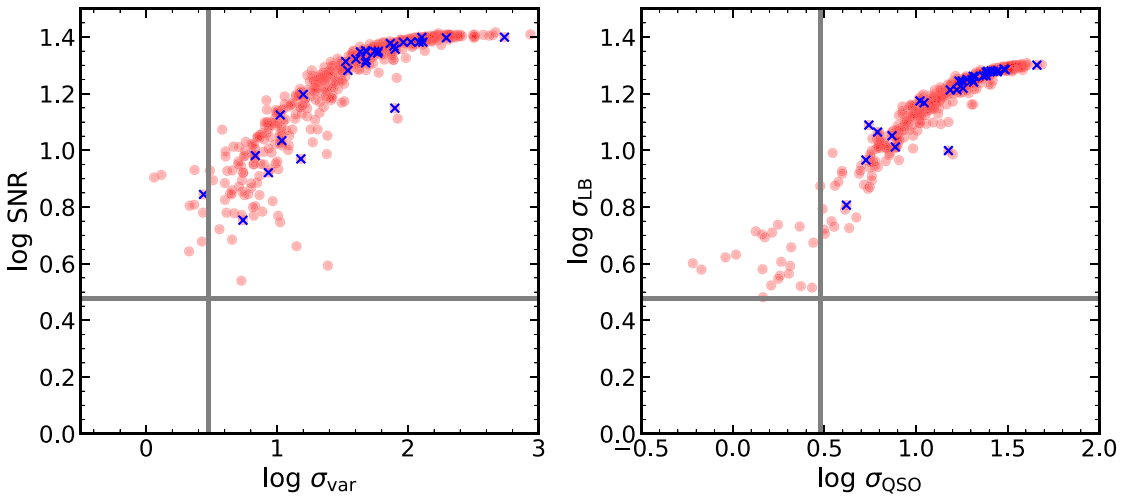

Figure 6. Comparison of variability significance criteria used in this work to the method of Butler & Bloom (2011) on DES light curves of galaxies. We plot the Shen et al. (2019) χ^2-based estimator (log SNR) used in this work versus the simple χ^2/ν variability significance (σ_{var}) of Butler & Bloom (2011) (left-hand panel). Galaxies with robustly estimated variability are located in the upper-right hand corner of the figure panel. We also plot the Ljung–Box test significance (σ_{LB}) used in this work versus the parametric quasar significance (σ_{QSO}) of Butler & Bloom (2011) (right-hand panel). Galaxies with AGN-like, correlated variability are located in the upper right-hand corner of the figure panel. The solid grey lines indicate 3σ thresholds; sources which pass both variability tests appear in the upper right-hand boxes in each panel. For clarity, only SN-C3 sources with SNR > 3 are shown. Sources with *Chandra* X-ray detections are shown as blue cross symbols.

constraint between different emission and absorption mechanisms across the EM spectrum. A large grid of models is computed and fitted to the data, allowing for an estimation of the star formation rate, stellar mass, and AGN contribution via a Bayesian-like analysis of the likelihood distribution. We use the z_{ph} values determined in Section 2.6 as input to CIGALE because CIGALE is not designed for z_{ph} inference, and indeed we found that the CIGALE photometric redshifts are much worse than the z_{ph} values using the method of Yang et al. (2017). We caution that the resulting stellar mass uncertainties do not include the additional uncertainty from the covariance between redshift and stellar mass. However, the systematic uncertainties due to model choices typically dominate (Ciesla et al. 2015; Boquien et al. 2019). In addition, variability contributes additional uncertainty in the SED shape over the quoted deep field photometry given the non-simultaneity of the observations between bands. Therefore, we sum the RMS variation of the *g*-band DES light curve in quadrature to the quoted photometric errors in the deep field photometric catalogue in all bands.

We use a delayed exponential star formation history and vary the e-folding time and age of the stellar population assuming a sub-solar metallicity (dwarf galaxies are expected to follow the mass metallicity relation; Kirby et al. 2013.) Studies of Local Group galaxies have shown that a delayed exponential model of star formation history is a good approximation for dwarf galaxies (Weisz et al. 2014). If a dwarf galaxy does not undergo merger induced burst of star formation, a single delayed exponential model may be reasonable. Furthermore, Zou et al. (2022) found that differences in star formation history result in systematic differences in stellar mass of only ∼0.1 dex for a sample of $z = 0 - 6$ AGN. We adopt the commonly used Chabrier (2003) initial stellar mass function with the stellar population models of Bruzual & Charlot (2003). We adopt the nebular emission template of Inoue (2011). We use the Leitherer et al. (2002) extension of the Calzetti et al. (2000) model for reddening due to dust extinction, and the Draine et al. (2014) updates to the Draine et al. (2007) model for dust emission. Finally, we adopt the SKIRTOR clumpy two-phase torus AGN emission model (Stalevski et al. 2012, 2016) allowing for additional polar extinction. We assume Type-1-like inclination angle varying from $i = 10^{o}$ to 30^{o} for galaxies with variable light curves (Section 2.5), while allowing the inclination angle to vary between $i = 40^{o}$ and 90^{o} for non-variable galaxies. Our choice of considering only a few viewing angles close to the average values for Type I and II AGNs is justified by previous studies, which found that different viewing angles were largely degenerate with the average values of 30^{o} and 70^{o} for Type I and II AGNs, respectively (e.g. Mountrichas et al. 2021; Ramos Padilla et al. 2022).

There is a strong degeneracy between blue colours from AGN UV-continuum emission and ongoing star formation in the SED of an AGN plus host galaxy. This presents considerable challenges when trying to estimate a stellar mass for our variable sample if the intrinsic AGN emission is mistakenly fit as the star formation component in CIGALE. To address this challenge, we fit each of our variable AGNs twice using CIGALE. First, instead of fixing the AGN fraction ($f_{\rm AGN}$) at 1 μm, we float this parameter to model star formation plus AGN, and we impose a bound of $0.2 < f_{\rm AGN} < 0.95$. Secondly, we set $f_{\rm AGN} = 0.9999$ to model an AGN-dominated SED (Yang et al. 2022). The lower limit of 0.2 is chosen as a conservative lower limit on the AGN luminosity fraction and is broadly consistent with variability of dwarf AGNs (Burke et al. 2022). We compute the reduced χ^2 values for each, and compute the difference $\Delta\chi^2_\nu = (\chi^2_\nu)_{f_{\rm AGN}=1} - \chi^2_\nu$. We interpret those SED with an improved fit when $f_{\rm AGN}$ is a free parameter to be sources with a significant contribution from star formation emission using the criteria $\Delta\chi^2_\nu > 2$. Because these sources have a significant star formation component in their SEDs, we consider their stellar masses to be reliable. On the other hand, sources with SEDs dominated by their AGN are unlikely to have a well-constrained star formation component, and therefore the stellar mass estimates are not reliable. We reject ∼1 per cent sources with a poor best-fitting model by requiring $\chi^2_\nu < 10$. The majority of the bad fits are sources with anomalous photometry or stars misclassified as galaxies.

A difficult problem is the degeneracy between low-redshift star-burst galaxies and high-redshift quasars with blue colours from AGN UV-continuum emission. Because we are interested in selecting variable dwarf galaxies, quasars incorrectly identified as low-redshift star-forming galaxies (which tend to be low mass) are a major contaminant. Fig. 7 demonstrates the effect of quasars with high redshifts incorrectly identified as dwarf galaxies. This branch of failures primarily occurs with high-redshift sources with incorrect photometric redshifts near $z_{\rm ph} \sim 0.1-0.4$, because of a colour degeneracy at these redshifts. These quasars have AGN power-law-dominated emission that are mostly rejected by our $\Delta\chi^2_\nu > 2$ constraint.

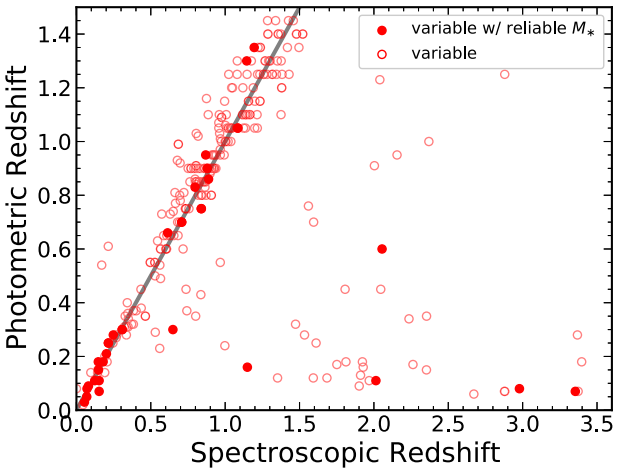

Figure 7. We show the photometric redshift versus spectroscopic redshift (when available) for variable galaxies in our sample (red circles). The solid grey line is the $y = x$ line. Catastrophic photo-z failures in the lower right-hand corner of the right panel are likely to be incorrectly identified as low stellar-mass galaxies by CIGALE. This is due to the degeneracy between the colours of low-z star-forming galaxies and high-z quasars. To remove most of these quasar interlopers, we reject sources that can be fit well with an AGN-dominated SED model, leaving sources with 'reliable' stellar mass estimates (solid red circles; see Section 2.7).

After this, the final parent sample of galaxies with well-sampled light curves and acceptable SED fits is 63,721. Of these, we find 706 variable galaxies, and 26 have $M_* < 10^{9.5}$ $M_\odot$ with reliable stellar mass estimates. The resulting distribution of stellar mass and redshift is shown in Fig. 8. To validate our SED fitting results, we compare our results in SN-C3 to matched sources with stellar masses and photometric redshifts from the FourStar Galaxy Evolution Survey (ZFOURGE; Tomczak et al. 2014; Straatman et al. 2016) in Appendix C. One concern is AGNs that are rejected using our AGN-dominated model comparison could be a function of stellar mass if the AGN-dominated source is more massive/less star forming. This bias may impact the variability fraction at larger stellar masses. Finally, we caution that additional systematic uncertainties on the stellar mass may be up to 20 per cent due to uncertainties in stellar evolution (e.g. initial mass function, star formation history) even when the photometric redshift is accurate (Ciesla et al. 2015; Boquien et al. 2019). This does not include additional sources of error from degeneracies between star formation and AGN light, for instance. Nevertheless, we check our photometric redshifts against spectroscopic redshifts available from the literature. The results are shown in Appendix C.

2.8 Variability analysis

To investigate the variability properties of our AGN candidates, we follow the Bayesian method of Kelly, Bechtold & Siemiginowska (2009) using a DRW prescription. The DRW is a common model which can describe the stochastic fluctuations in AGN optical light curves, which may result from thermal fluctuations in the accretion disc. The simple DRW model includes both an amplitude SF_∞ and characteristic (damping) variability time-scale term $\tau_{\rm DRW}$. We use the

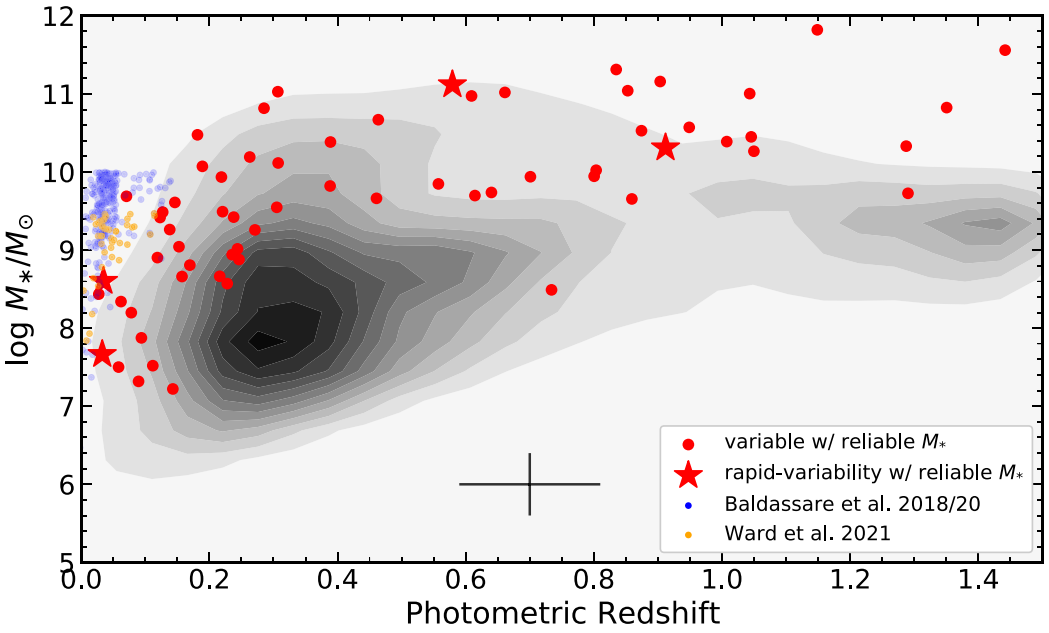

Figure 8. Stellar mass versus photometric redshift for variable (red symbols) and non-variable (black contours) galaxies in our DES deep field sample with 'reliable' stellar mass estimates (see Section 2.7 for details). The sources with rapid optical variability in Table 3 are shown as red star symbols. The typical (mean) uncertainties in stellar mass and redshift are shown at the bottom of the plot. For comparison, we show the variability-selected dwarf AGNs from SDSS/PTF (blue dots; Baldassare et al. 2018, 2020) and ZTF imaging (orange dots; Ward et al. 2021a). Our deep-field variability-selected AGNs are at relatively lower mass at a given redshift than previous optically selected AGNs. This can only be matched by deep X-ray/radio imaging (Guo et al. 2020).

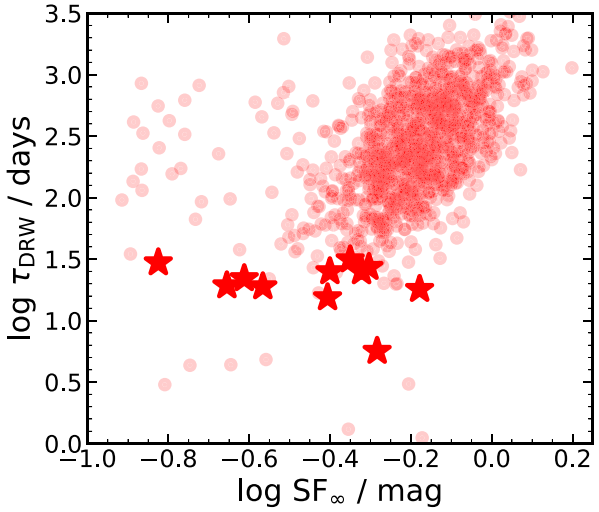

Figure 9. Rest-frame damping time-scale $\tau_{\rm DRW}$ versus asymptotic variability amplitude SF_∞ for our AGN candidates. The sources with rapid optical variability with constrained damping time-scales in Table 3 are shown as red star symbols.

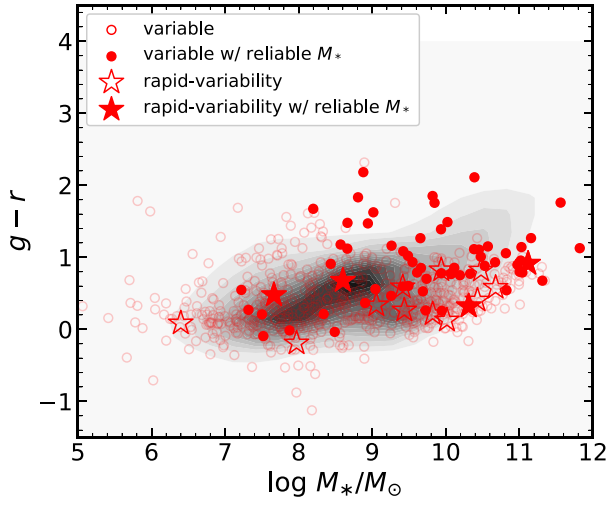

Figure 10. Galaxy $g-r$ colours versus stellar mass for variable (red) and non-variable (black contours) sources. The variable galaxies tend to be somewhat bluer at given stellar mass.

Gaussian process DRW prescription following Burke et al. (2021), which makes use of the CELERITE (Foreman-Mackey et al. 2017) and EMCEE (Foreman-Mackey et al. 2013) codes. The amplitude−rest-frame time-scale distribution of our sources is shown in Fig. 9.

Recently, Burke et al. (2021) identified a scaling relation between the characteristic time-scale and BH mass using AGN light curves. This enables a BH mass estimate independent of spectroscopic techniques or via indirect stellar mass estimation using SED fitting, which can suffer from strong model degeneracies or rely on the BH–host scaling relations which are still poorly constrained in dwarf galaxies particularly at high redshift. The relation is given by

$$M_{\rm BH} = 10^{7.97^{+0.14}_{-0.14}}\ {\rm M}_\odot \left(\frac{\tau_{\rm DRW}}{100\ {\rm days}}\right)^{2.54^{+0.34}_{-0.35}}, \qquad (10)$$

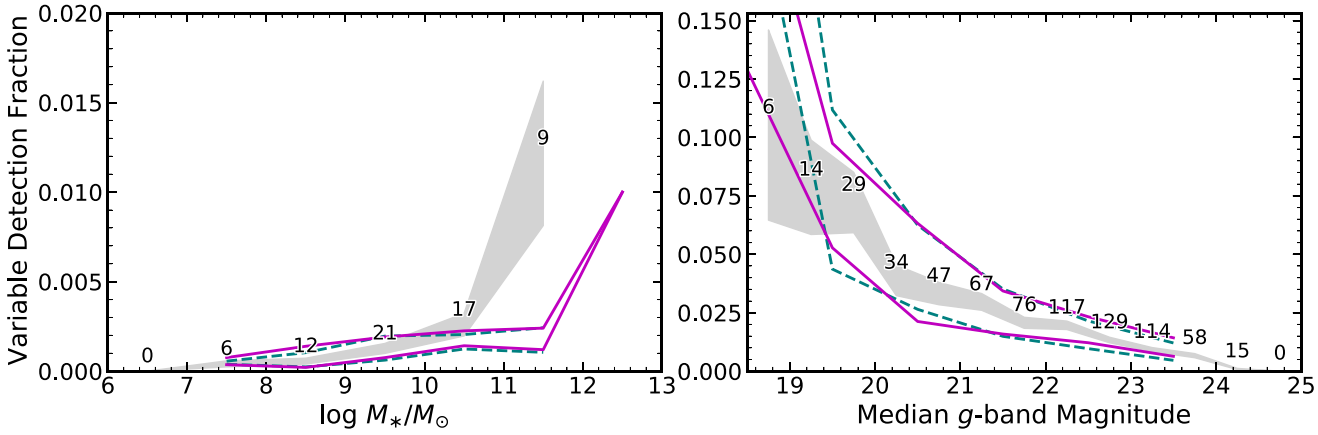

Figure 11. Fraction of variable AGN versus stellar mass (left-hand panel) and median g-band apparent magnitude (right-hand panel). The grey shaded areas are the 1σ bands of uncertainty for each bin computed assuming a binomial distribution. The number of variable galaxies in each bin is given above each bin. The magenta lines are the predicted detection fractions assuming a model with a constant occupation fraction of 1 (the most optimistic 'light' seed scenario). The green dashed lines are the predictions assuming an occupation fraction which drops dramatically below $M_* = 10^8$ $M_\odot$ (the 'heavy' seed scenario; Ricarte & Natarajan 2018; Bellovary et al. 2019), as described by Burke et al. (2022) for central BHs (see Section 3.1 for details). We caution that the bright end with $g \lesssim 18$ mag and $M_* \gtrsim 10^{10.5}$ $M_\odot$ is highly incomplete and our model and observations differ.

with an intrinsic scatter of 0.33 ± 0.11 dex in $M_{\rm BH}$. Therefore, a reasonable variability constraint for dwarf AGN identification is $\log(\tau_{\rm DRW}/{\rm days}) \leq 1.5$, which corresponds to $M_{\rm BH} \lesssim 5 \times 10^6$ $M_\odot$. We also impose a requirement that the observed-frame damping time-scale be larger than the observed cadence to avoid unconstrained values. Finally, we caution that the damping time-scales for some of our sources may be biased smaller to due insufficient light-curve duration (Kozłowski 2017). This is unlikely to affect our dwarf AGNs, whose damping time-scales are typically less than 10 times the light-curve baseline. Finally, we note this relation has some scatter that we are selecting against which can result in a large scatter in the resulting stellar masses, even if they are reliable due to the 0.5 dex scatter in the host galaxy–BH mass scaling relations (Reines & Volonteri 2015). One source, J033051.6−272856.2 has an apparently anomalously large stellar mass ($M_* \sim 10^{11}$ $M_\odot$) but its SED has a large contribution from AGN emission which could bias the stellar mass larger (see Fig. 12).

3 RESULTS

3.1 Detection fraction

We select 706 variable AGN candidates out of 63 721 total galaxies. We find 26 AGNs in low stellar mass $M_* < 10^{9.5}$ $M_\odot$ galaxies with reliable stellar mass estimates. We show their optical colours versus stellar mass in Fig. 10. The stellar mass versus redshift of our variability-selected candidates are shown in Fig. 8. We plot the fraction of variability-selected AGNs versus magnitude and stellar mass in Fig. 11. However, the variable AGN detection fraction is influenced by a selection bias of variability being more difficult to detect in fainter sources. However, an understanding of the constraints on the occupation fraction from the observed AGN variability fraction requires a comprehensive demographic model of the true variable AGN population combined with physically motivated AGN light-curve simulations to capture the selection effects related to the survey sensitivity, depth, and light-curve sampling.

We attempt to quantify these effects using the forward Monte Carlo sampling model of Burke et al. (2022). This model generates mock light curves for a given instrument from a population of variable AGNs drawn from 'light' and 'heavy' seeding scenarios (e.g. Ricarte & Natarajan 2018; Bellovary et al. 2019) using an input galaxy stellar mass function, Eddington ratio distribution function, obscured AGN fraction, and constrains on AGN variability behaviour from observations. We input the DES-SN-like survey parameters (six-year baseline, 7-d cadence) using the typical photometric precision shown in Appendix A. We do not include off-nuclear variable BHs in our comparison because our study is restricted to nuclear variability. It is unclear how the off-nuclear IMBH population, which could make up a larger fraction of AGNs in dwarf galaxies, could be connected to their host galaxy stellar mass (e.g. Greene et al. 2020) A stellar mass uncertainty of 0.6 dex is assumed in our model prediction. The distinguishing power between the two occupation fractions lies in the shapes of the variability fractions in Fig. 11. We re-normalized the detection fractions by an arbitrary scaling to match our detection fraction, because we have removed a large fraction of variable sources with unconstrained stellar mass estimates. Our variable fraction is lower than some previous works (Baldassare et al. 2020) but more consistent with Baldassare et al. (2018). This is, in part, dependent on the limiting redshift of the parent sample. Given the limited number of variable sources with reliable stellar masses in the 4.6 deg^2 in this work, our model predictions are unable to distinguish between the two occupation fractions for the different 'light' and 'heavy' seeding scenarios. Hence, we are unable to put strong constraints on the occupation fraction at this time. Future work including a larger area with greater number statistics may be more promising. Nevertheless, we have demonstrated the feasibility of using deep fields to explore the variable dwarf AGN population.

3.2 Dwarf AGN Candidates

We present a catalogue of all of our variability-selected AGN candidates in Table 2 regardless of stellar mass or variability properties. We list the source name, coordinates, median g-band magnitude, variability statistics (SNR and $\sigma_{\rm LB}$), stellar mass estimate, and damping time-scale $\tau_{\rm DRW}$. If available from supplementary catalogues, we include the spectroscopic redshift $z_{\rm sp}$ and the source

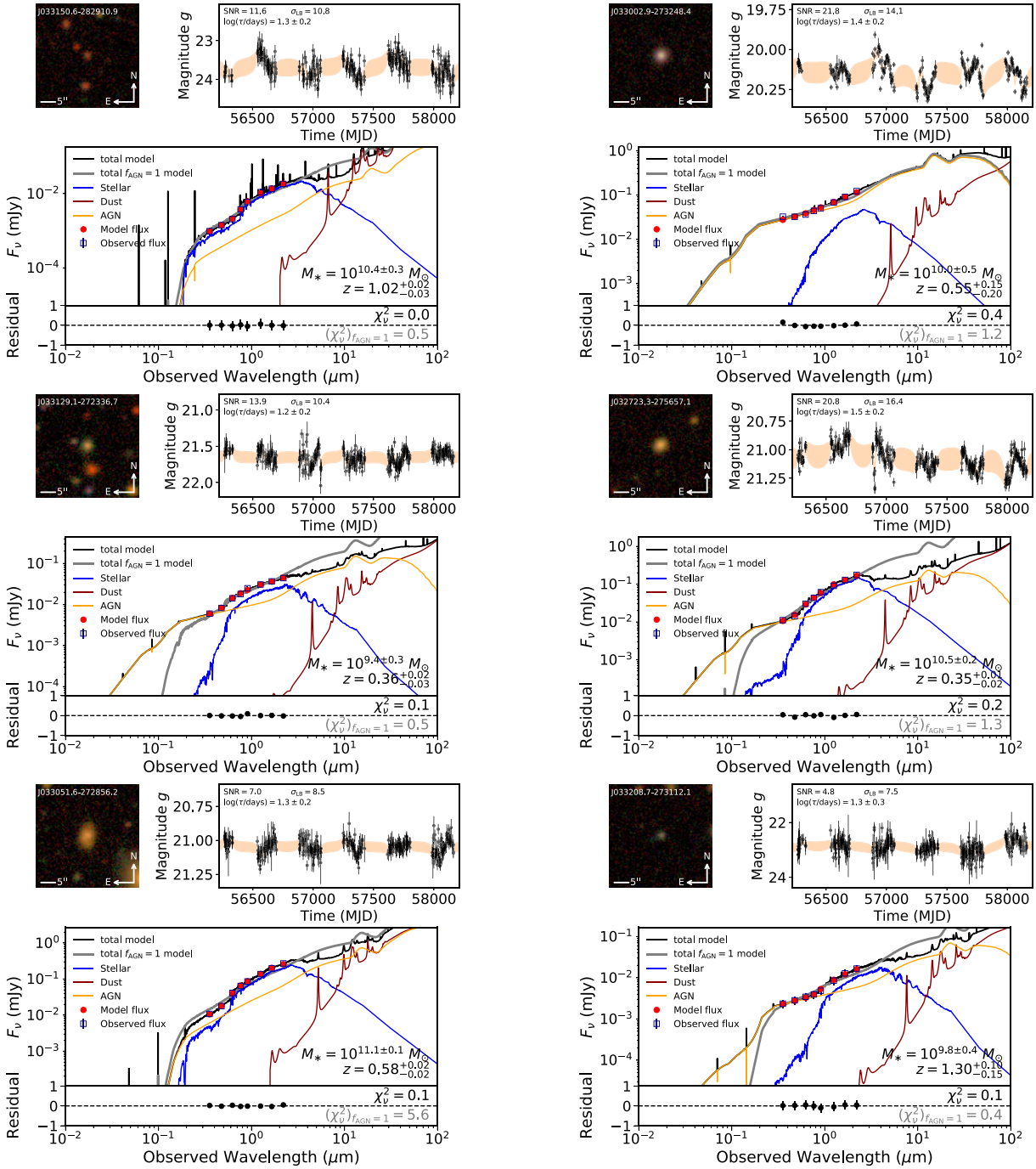

Figure 12. Candidate variability-selected dwarf AGNs from Table 3. We show the DES *gri* colour-composite coadd (top left-hand panel). The coadd image is stacked to the six-year DES-wide field depth. We also show the *g*-band light curve as black points with the 1σ error ellipse from the DRW modelling in orange (top right-hand panel) and best-fitting CIGALE SED fitting results (bottom panel). The observed photometry is shown as blue squares. The best-fit model photometry is shown as red points. The best-fitting AGN+star-forming model (allowing f_{AGN} to be a free parameter) is shown in black, while the best-fitting AGN-dominated model (fixing $f_{AGN} = 1$) is shown in grey. The components from attenuated stellar emission (blue), dust emission (red), and the AGN emission (orange) are also shown. A nebular emission component is also fit, but its component is not shown for clarity. The estimated stellar mass and photometric redshift are shown in the lower right of the panel, but the stellar mass uncertainties are likely underestimated for reasons described in Section 2.7. The relative residual flux [(observed − model)/observed] is shown at the bottom of each panel along with the χ^2_ν for the AGN+star-forming model (black) and AGN-dominated model (grey). A larger $(\chi^2_\nu)_{f_{AGN}=1}$ value indicates there is a significant star formation component in the SED and that the stellar mass estimate is likely more reliable.

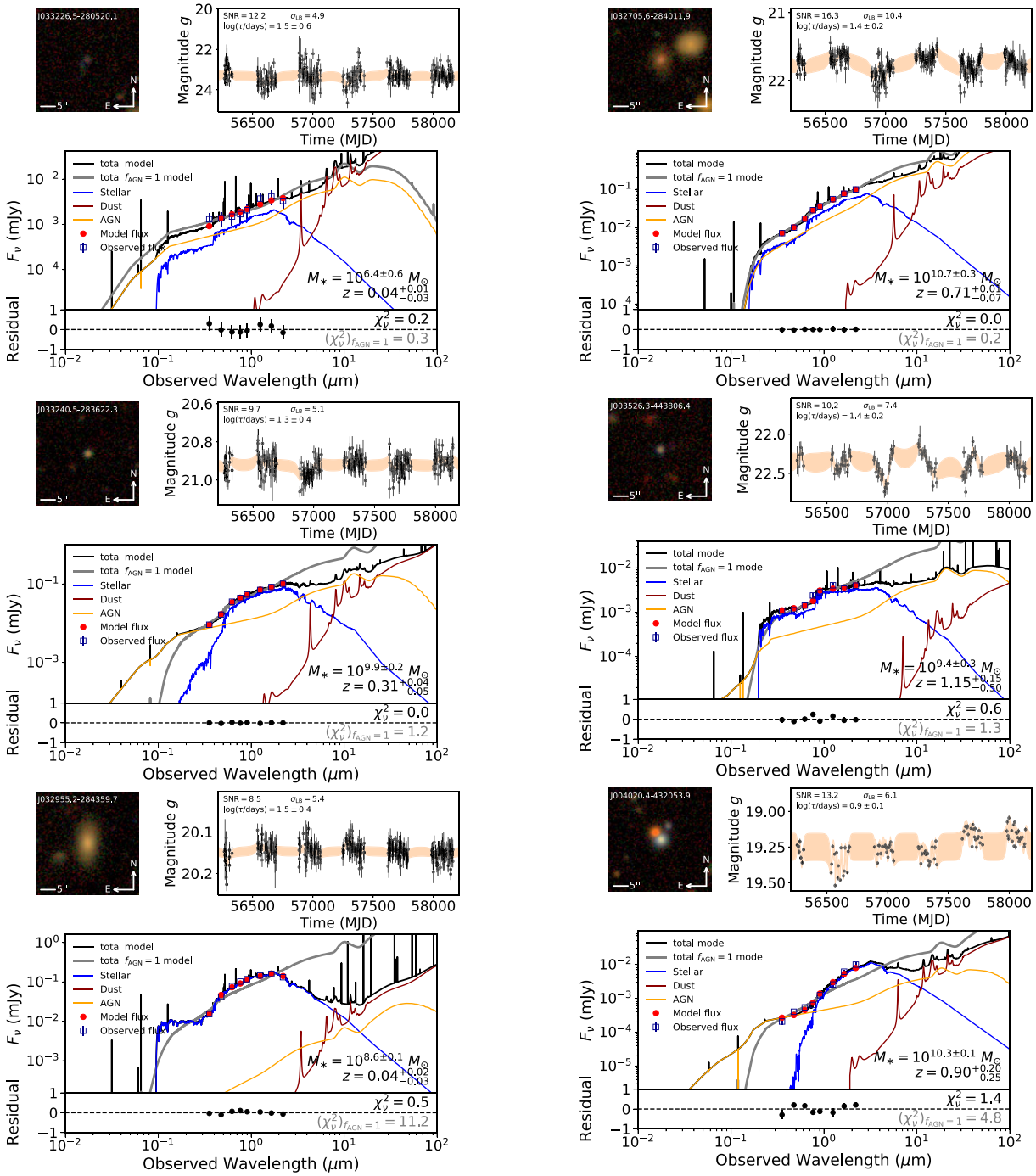

Figure 12 – *continued*

of z_{sp}. When available, we also include supplementary *WISE* $W1 - W2$ colours and the *Chandra* Source Catalogue hard X-ray flux. Finally, we list the DES deep field that contains the source. The stellar mass estimates should be treated with caution for reasons described in Section 2.7. Therefore, we present a subset of this catalogue in Table 3, which includes only those AGN candidates with rapid characteristic variability time-scales, defined as rest-frame $\log(\tau_{DRW}/\text{days}) < 1.5$ with observed-frame damping time-scales greater than the 7-d cadence. Most of the 15 sources have stellar masses below 10^{10} $M_\odot$. We show our dwarf AGN candidate images, light curves, and SED-fitting analysis for the candidates with rapid variability in Table 3 in Fig. 12. This strict criteria are expected to result in a pure selection of dwarf AGNs given the at least ∼0.3 dex scatter in the Burke et al. (2021) relation and large uncertainties on the individual damping time-scale measurements (∼0.4 dex or larger depending on the ratio of the damping time-scale to the light-curve baseline), so results in much fewer candidates compared to the stellar mass criteria. Indeed, if we relax the damping time-scale constraint to rest-frame $\log(\tau_{DRW}/\text{days}) < 2.3$ with no floor at the light-curve cadence, we find ∼150 sources. We found 17 sources with observed-frame damping time-scales less than 7 d, which could be interpreted as an upper limit on the true damping time-scale or sources

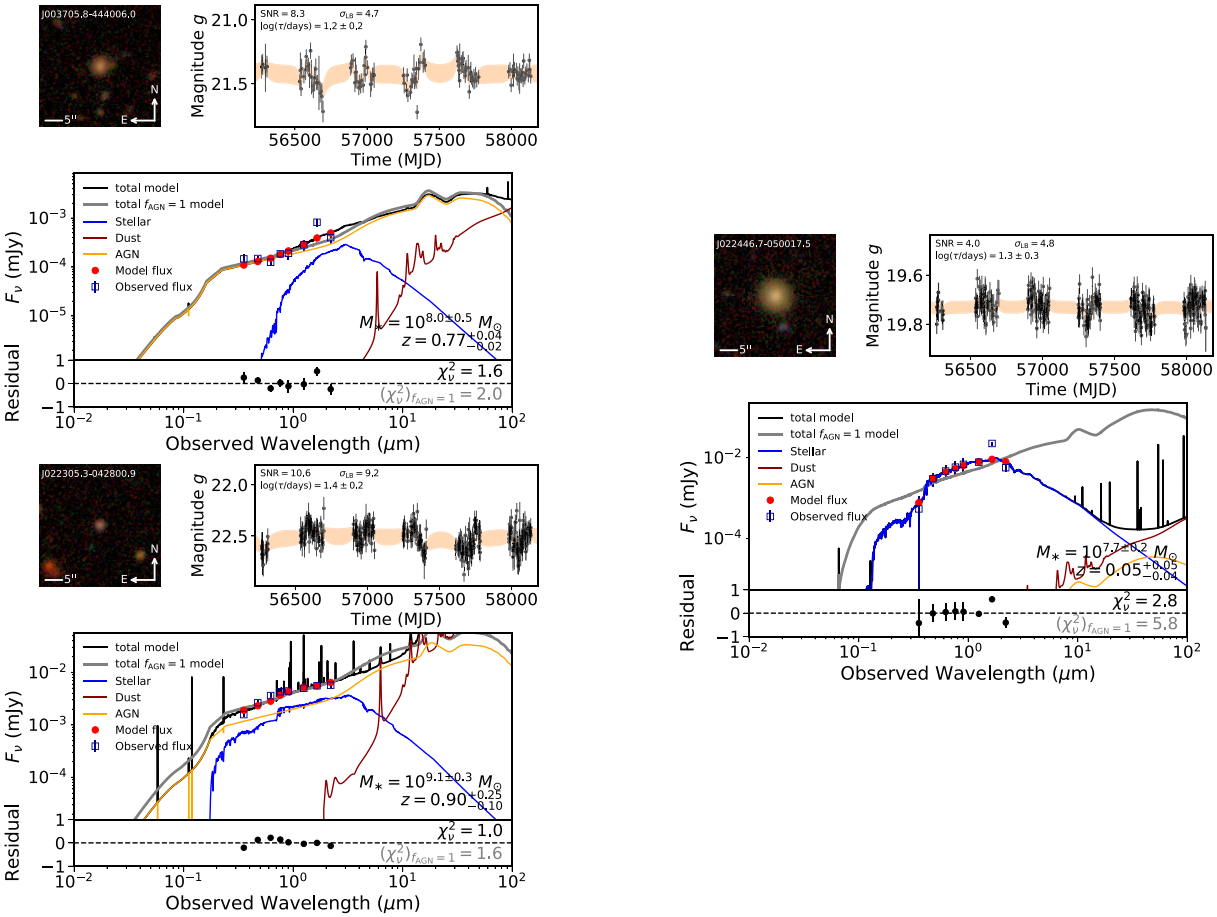

Figure 12 – *continued*

Table 2. Full catalogue of 706 variable AGN candidates regardless of stellar mass or variability time-scale. All coordinates are given in the J2000 epoch. Values of −1 indicate invalid values. The first five rows are shown for formatting guidance. A full version of this table is available in the online version.

Name	RA (°)	Dec. (°)	g (mag)	SNR	σ_{LB}	log $\frac{M_*}{M_\odot}$ (dex)	$\Delta\chi^2_\nu$	log $\frac{\tau_{DRW,rest}}{days}$ (dex)	z_{ph}	z_{sp}	z_{sp} source	$W1-W2$	log $\frac{F_{2-7\,keV}}{erg\ s^{-1}\ cm^{-2}}$ (dex)	Field
032833.79-271056.42	52.1408	−27.1823	23.7	14.2	13.3	10.1 ± 0.4	0.1	3.2 ± 0.6	$1.02^{+0.03}_{-0.04}$	NaN	None	0.4	NaN	SN-C3
J032951.20-271057.43	52.4633	−27.1826	23.4	15.3	12.7	7.8 ± 0.7	0.1	1.9 ± 0.3	$0.24^{+0.04}_{-0.02}$	NaN	None	18.6	NaN	SN-C3
J032944.64-271107.53	52.4360	−27.1854	23.4	20.1	16.3	9.4 ± 0.5	0.0	2.4 ± 0.8	$1.09^{+0.02}_{-0.02}$	NaN	None	0.9	NaN	SN-C3
J032845.45-271117.18	52.1894	−27.1881	21.5	22.8	18.3	9.7 ± 0.0	5.0	1.7 ± 0.2	$1.30^{+0.10}_{-0.15}$	NaN	None	1.1	NaN	SN-C3
J032843.19-271117.75	52.1799	−27.1883	23.8	13.4	12.4	8.8 ± 0.5	0.0	2.7 ± 0.8	$0.60^{+0.25}_{-0.05}$	NaN	None	NaN	NaN	SN-C3
...	...	...	...	...	...	...	...	...	...	...	...	...	...	...

whose variability is statistically spurious or not characteristic of an AGN.

3.3 Spectroscopic properties

Three of our sources with rapid variability in Table 3, J033129.06−272336.65, J032723.33−275657.10, and J033240.53−283622.28 have 2dF spectra from the OzDES[2] program (Lidman et al. 2020). One source, J033129.06–272336.65, shows possible absorption features but no clear emission lines, which may indicate the AGN emission is diluted by absorption from an old stellar population. J032723.33−275657.10 and J033240.53−283622.28 do not show strong emission or absorption features. These sources are faint $g \sim 21$, and probably require higher S/N spectra. Another source, J022446.71−050017.47, has a spectrum from the Pan-STARRS SN sample (Rest et al. 2014), but its spectrum would be contaminated by SN emission.

3.3.1 J022305.3-042800.9

We identified one source with short-time-scale variability in Table 3, J022305.3-042800.9 (see Fig. 12), with a good SDSS spectrum. The stellar mass of the source is $M_* = 10^{9.1} \pm 10^{0.3}\,M_\odot$ and its $z_{ph} = 0.90^{+0.25}_{-0.10}$ is consistent with the spectroscopic redshift of $z_{sp} = 0.8194$. The calibrated SDSS spectra enables straightforward spectral modelling using existing tools. This source is of class 'QSO' and shows broad Hβ and Mg II emission lines. We will use the broad lines to obtain single-epoch virial BH mass estimates.

[2]Australian Dark Energy Survey

Table 3. Catalogue of 15 variable AGN candidates with rapid variability (log ($\tau_{\rm DRW}$/days) < 1.5). We consider these sources the best dwarf AGN candidates. All coordinates are given in the J2000 epoch. Values of −1 indicate invalid values.

Name	RA (°)	Dec. (°)	g (mag)	SNR	$\sigma_{\rm LB}$	log $\frac{M_*}{M_\odot}$ (dex)	$\Delta\chi^2_\nu$	log $\frac{\tau_{\rm DRW,rest}}{\rm days}$ (dex)	$z_{\rm ph}$	$z_{\rm sp}$	$z_{\rm sp}$ source	$W1-W2$	log $\frac{F_{2-7\ \rm keV}}{\rm erg\ s^{-1}\ cm^{-2}}$ (dex)	Field
J033150.63-282910.86	52.9610	−28.4863	23.7	11.6	10.8	10.4 ± 0.3	0.4	1.2 ± 0.2	$1.02^{+0.02}_{-0.03}$	NaN	None	22.5	NaN	SN-C3
J033129.06-272336.65	52.8711	−27.3935	21.6	13.9	10.4	9.4 ± 0.3	0.4	1.2 ± 0.2	$0.36^{+0.02}_{-0.03}$	0.3456	2dF	0.6	NaN	SN-C3
J033051.65-272856.18	52.7152	−27.4823	21.0	7.0	8.5	11.1 ± 0.1	5.5	1.3 ± 0.2	$0.58^{+0.02}_{-0.02}$	NaN	None	0.5	NaN	SN-C3
J033002.95-273248.41	52.5123	−27.5468	20.1	21.8	14.1	10.0 ± 0.5	0.8	1.4 ± 0.2	$0.55^{+0.15}_{-0.20}$	0.5270	2dF	0.7	NaN	SN-C3
J032723.33-275657.10	51.8472	−27.9492	21.1	20.8	16.4	10.5 ± 0.2	1.1	1.5 ± 0.2	$0.35^{+0.01}_{-0.02}$	0.4635	2dF	0.6	NaN	SN-C3
J033208.67-273112.08	53.0361	−27.5200	22.9	4.8	7.5	9.8 ± 0.4	0.4	1.3 ± 0.3	$1.30^{+0.10}_{-0.15}$	NaN	None	17.8	NaN	SN-C3
J033226.49-280520.08	53.1104	−28.0889	23.3	12.2	4.9	6.4 ± 0.6	0.0	1.5 ± 0.7	$0.04^{+0.01}_{-0.03}$	NaN	None	NaN	NaN	SN-C3
J033240.53-283622.28	53.1689	−28.6062	20.9	9.7	5.1	9.9 ± 0.2	1.1	1.3 ± 0.4	$0.31^{+0.04}_{-0.05}$	0.3224	2dF	0.3	NaN	SN-C3
J032955.16-284359.67	52.4798	−28.7332	20.1	8.5	5.4	8.6 ± 0.1	10.7	1.5 ± 0.4	$0.04^{+0.02}_{-0.03}$	NaN	None	−0.1	NaN	SN-C3
J032705.57-284011.91	51.7732	−28.6700	21.7	16.3	10.4	10.7 ± 0.3	0.2	1.4 ± 0.2	$0.71^{+0.01}_{-0.07}$	NaN	None	0.2	NaN	SN-C3
J003526.35-443806.37	8.8598	−44.6351	22.4	10.2	7.4	9.4 ± 0.3	0.7	1.4 ± 0.2	$1.15^{+0.15}_{-0.50}$	NaN	None	17.3	NaN	SN-E2
J004020.38-432053.86	10.0849	−43.3483	19.2	13.2	6.1	10.3 ± 0.1	3.5	0.9 ± 0.1	$0.90^{+0.20}_{-0.25}$	NaN	None	1.2	NaN	SN-E2
J003705.78-444006.02	9.2741	−44.6683	21.4	8.3	4.7	8.0 ± 0.5	0.4	1.2 ± 0.2	$0.77^{+0.04}_{-0.02}$	NaN	None	0.2	NaN	SN-E2
J022305.26-042800.90	35.7719	−4.4669	22.5	10.6	9.2	9.1 ± 0.3	0.6	1.4 ± 0.2	$0.90^{+0.25}_{-0.10}$	0.8194	SDSS	0.7	NaN	SN-X3
J022446.71-050017.47	36.1946	−5.0049	19.7	4.0	4.8	7.7 ± 0.2	3.1	1.3 ± 0.3	$0.05^{+0.05}_{-0.04}$	0.0694	PanS	0.1	NaN	SN-X3

To determine the significance of the broad emission lines and to measure their profiles for virial BH mass estimates, we fit spectral models following the procedures as described in detail in Shen et al. (2019) using the software PyQSOFit[3] (Guo, Shen & Wang 2018). The model is a linear combination of a power-law continuum, a third-order polynomial (to account for reddening), a pseudo continuum constructed from Fe II emission templates, and single or multiple Gaussians for the emission lines. Since uncertainties in the continuum model may induce subtle effects on measurements for weak emission lines, we first perform a global fit to the emission-line free region to better quantify the continuum. We then fit multiple Gaussian models to the continuum-subtracted spectrum around the broad emission line region locally.

More specifically, we model the Mg II and Hβ lines each using a single broad (FWHM >1200 km s^{-1}) Gaussian component. Given the low S/N of the spectrum, adding additional components does not improve the fit significantly. The [O III] λ5007 Å emission line appears affected by skyline residuals. Therefore, we are unable to use it as a template to tie the narrow components. This contributes to the large uncertainties in our virial mass measurements. We use 100 Monte Carlo simulations to estimate the uncertainty in the line measurements.

Our spectral modelling is shown in Fig. 13. Using the virial mass relation (Shen 2013),

$$\log\left(\frac{M_{\rm BH}}{M_\odot}\right) = a + b\log\left(\frac{\lambda L_\lambda}{10^{44}\ {\rm erg\ s^{-1}}}\right) + 2\log\left(\frac{\rm FWHM}{\rm km\ s^{-1}}\right), \quad (11)$$

we obtain BH mass estimates of $\log(M_{\rm BH}/{\rm M}_\odot) = 6.4 \pm 0.6$ (Hβ) and $\log(M_{\rm BH}/{\rm M}_\odot) = 6.6 \pm 0.1$ Mg II using the relations of Mejía-Restrepo et al. (2016) with (a, b) = (0.864, 0.568) (Hβ) and (a, b) = (0.955, 0.599) (Mg II). The redshift and BH mass are similar to the source of Guo et al. (2018), which is not within one of the deep NIR fields of this work. Although the BH mass is somewhat larger than other samples (e.g. Reines, Greene & Geha 2013), those samples are generally limited to low redshifts ($z \lesssim 0.15$). This demonstrates the capability of variability to identify lower mass SMBHs at intermediate redshifts. Both values are consistent with the predicted $\log(M_{\rm BH}/{\rm M}_\odot) = 6.4 \pm 0.4$ from the $M_{\rm BH}-\tau_{\rm DRW}$ of Burke et al. (2021).

[3]https://github.com/legolason/PyQSOFit

4 DISCUSSION

4.1 Comparison to previous works

Baldassare et al. (2018, 2020) used the Butler & Bloom (2011) method to select dwarf AGNs ($M_* < 10^{10}\,{\rm M}_\odot$) in SDSS Stripe 82 and Palomar Transient Factory light curves, respectively, using difference imaging. The variable AGN fraction found in these works is broadly consistent with our findings ($\lesssim 1$ per cent) given the different cadence, baselines, and photometric precision between surveys. A similar work was performed using Zwicky Transient Facility imaging (Ward et al. 2021a). We have extended the findings of Baldassare et al. (2020), showing that the occupation fraction of variable AGNs may be constant down to $M_* \sim 10^7\,{\rm M}_\odot$. These earlier studies are restricted to samples of galaxies at $z < 0.15$ with secure spectroscopic redshifts. In this work, we are able to extend the results to a sample at higher redshifts than Baldassare et al. (2018, 2020). Although we caution that our stellar masses are likely more uncertain due to the larger uncertainties in the photometric redshifts and lack of deep UV and MIR photometry.

As an additional point of comparison, we plot the stellar mass versus redshift against the sample of dwarf AGN selected from the *Chandra* COSMOS legacy survey (Mezcua et al. 2018) in Fig. 14. This demonstrates that our variability-selected AGN has comparable redshifts and stellar masses to the deep X-ray AGN selection technique. This is consistent with fig. 7 of Guo et al. (2020), which showed that DES-SN variability selection can only be matched by deep X-ray/radio imaging in the mass–redshift parameter space. In contrast, our technique covers a much larger area of the sky, but will miss Type II AGN with variability obscured in the optical.

4.2 X-ray properties

We match our sources to the *Chandra* Source Catalogue 2.0 (Evans et al. 2010) of X-ray sources. This catalogue includes detections in stacked observations in the *Chandra* Deep Field South with a 5.8 Ms total exposure time. We matched our DES sources to this catalogue using a 0.5 arcsec radius. We found 105 X-ray sources with variable DES light curves.

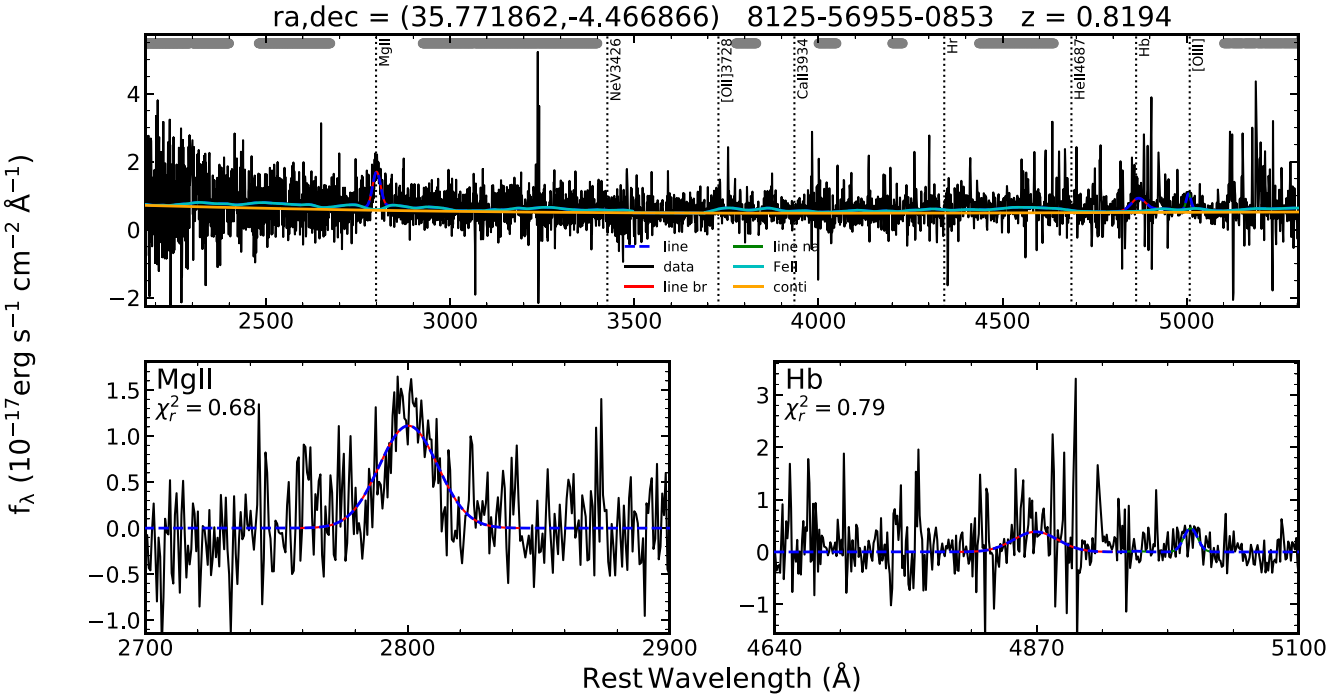

Figure 13. Optical spectrum for example source J022305.3−042800.9 from SDSS. A global fitting is applied to the spectrum having subtracted the host component in the upper panel. A power-law plus third-order polynomial and Gaussians are used to fit the continuum and emission lines, respectively. The grey bands on the top are line-free windows selected to determine the continuum emission. The lower panels show the zoomed-in emission line regions of Mg II and Hβ. Broad Mg II and broad Hβ are both detected at the 3.5σ and 1.2σ significance levels, respectively, yielding virial BH mass of $\log(M_{\rm BH}/M_\odot) = 6.4 \pm 0.6$ M$_\odot$ using Hβ and $\log(M_{\rm BH}/M_\odot) = 6.6 \pm 0.1$ using Mg II.

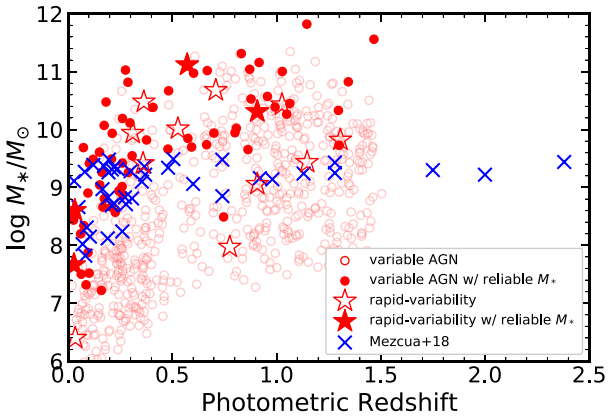

Figure 14. Stellar mass versus photometric redshift for variable galaxies in our DES deep field sample with reliable stellar mass estimate (red). The sources with rapid optical variability in Table 3 are shown as red star symbols. The typical (mean) uncertainties in stellar mass and redshift are shown at the bottom of the plot. For comparison, we show the X-ray-selected dwarf AGNs from *Chandra* COSMOS legacy survey imaging (Mezcua et al. 2018).

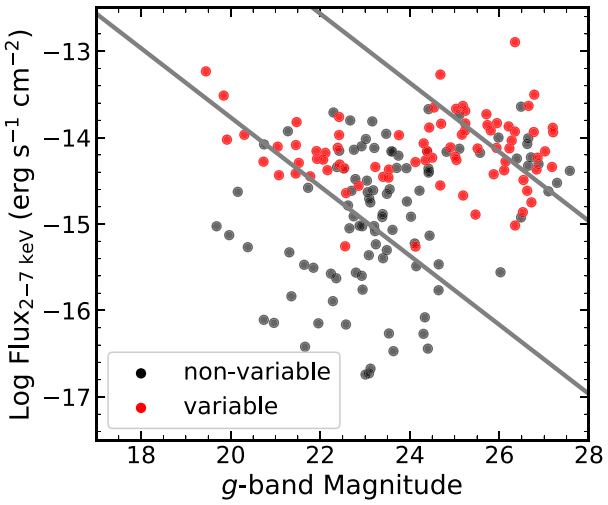

Figure 15. *Chandra* hard (2−7 keV) X-ray flux versus g-band magnitude for variable (red) and non-variable (black) galaxies. The grey lines correspond to X-ray to optical flux ratios of $X/O = \pm 1$.

We compute the X-ray to optical flux ratio X/O of our sources in the *Chandra* Deep Field South. We use the definition of Maccacaro et al. (1988):

$$X/O = \log(f_X/f_{\rm opt}) = \log f_x + \frac{\rm mag_{opt}}{2.5} + C, \quad (12)$$

where $f_{\rm X}$ is the X-ray flux (we use the *Chandra* hard X-ray band 2−7 keV), $\rm mag_{opt}$ is the optical magnitude (we use the g-band deep coadd photometry), and C is a zero-point constant ($C = 4.77$ for the g band). The results are shown in Figs 15 and 16 for sources with acceptable stellar mass estimates. The non-variable sources with X-ray detections are likely optically obscured AGN. In addition, sources may have significant contamination from star formation. Nevertheless, the fact that all variable sources fall near or above the $X/O = -1$ line reassures that the variability in most of our sources is of AGN nature.

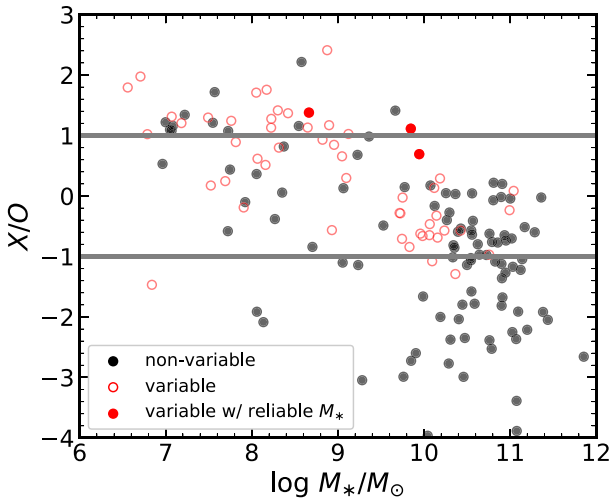

Figure 16. X-ray to optical flux ratio versus stellar mass for variable (red) and non-variable (black) galaxies. The grey lines correspond to X-ray to optical flux ratios of $X/O = \pm 1$.

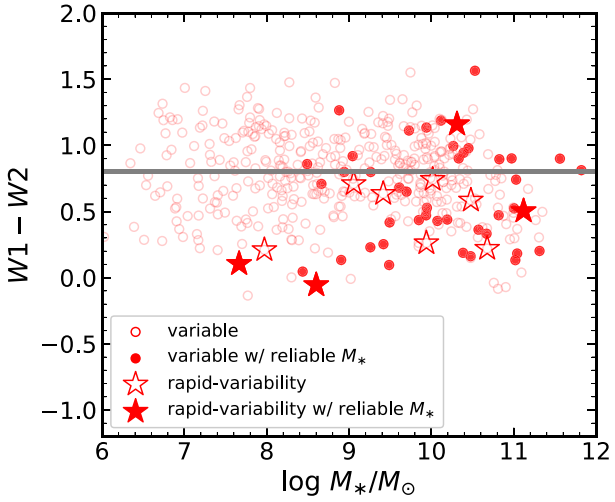

Figure 17. *WISE* $W1 - W2$ colours versus stellar mass for variable sources. The grey line is the simple threshold for AGN selection of $W1 - W2 > 0.8$ proposed by Stern et al. (2012).

Only three of the AGN candidates with rapid optical variability time-scales in Table 3 appear to be on an archival *Chandra* observation, and none of those candidates is present in the *Chandra* Source Catalogue 2.0. As such we search for X-ray counterparts in the observations of another X-ray telescope, *XMM*–Newton, by using the processed data and region files of the *XMM* cluster survey (XCS, Romer et al. 2001). XCS is a serendipitous survey of the *XMM* data archive that is primarily focused on the measurement of galaxy cluster properties, but also locates and catalogues X-ray point sources. The XCS source finder (XAPA) first locates X-ray sources in *XMM* data, and then classifies their emission as point or extended.

We use X-ray: Generate and Analyse (XGA,[4] Turner et al. 2022); a new, open-source, X-ray astronomy analysis module developed by XCS, to first determine which of the candidates in Table 3 have *XMM* data, and then which of those candidates match to an XCS point source. We find that all of the 11 candidates appear in at least one *XMM* observation, with the most well-observed candidates appearing in eight. We also find that 6 of the 11 have a corresponding XCS point source match in at least one *XMM* observation, where we define a match as the DES coordinate falling within an XCS point source region. We use XGA to generate stacked *XMM* count-rate maps, both with and without spatially varying PSF correction; as the sample in Table 3 is small, visual inspection to confirm the veracity of the matches is possible. In one case, we note what appears to be very faint point source emission at the coordinates of the candidate, with no corresponding XCS source region. In all other cases, the detections and non-detections appear to be appropriate. The notebook containing the brief *XMM* analysis is available on GitHub.[5]

We also check the 4XMM DR11 catalogue (Webb et al. 2020), and find that 7 of the 11 candidates match to a 4XMM source within 3 arcsec, 6 of which are detected by XCS. The additional candidate detected by 4XMM is the same one for which we note a slight emission during visual inspection. The lack of detection is likely caused by XCS performing source finding in the 0.5–2.0-keV band, which is optimized for the detection of galaxy clusters. We defer the full X-ray analysis of our variability-selected AGN sample to a future paper.

4.3 *WISE* properties

We match our variable AGN candidates to the all-sky unWISE extragalactic catalogue (Schlafly, Meisner & Green 2019) using a 5 arcsec radius which includes both galaxies and AGNs. We find 389 matches that satisfy the simple *WISE* AGN selection criteria of $W1 - W2 > 0.8$ (Stern et al. 2012) out of 706 total matches. We plot the $W1 - W2$ colours versus stellar mass in Fig. 17 for sources with acceptable stellar mass estimates. The colours follow the upper-tail of the $W1 - W2$ distribution for galaxies and AGNs (Stern et al. 2012; Assef et al. 2013), suggesting some AGN contribution to the MIR emission. Nevertheless, this demonstrates that a large fraction (∼50 per cent) of our variable AGN sources are not dominated by AGN emission in the MIR. Hence, these variable AGN would be missed by MIR colour selection.

4.4 Comparison to host scaling relations

We show the BH masses estimated from the damping time-scales using the relation of Burke et al. (2021) versus host galaxy stellar mass estimates from CIGALE SED fitting for our 15 sources with rapid optical variability in Table 3 in Fig. 18. Shown for comparison is best-fitting relation from the X-ray selected AGN sample at median $z \sim 0.8$ from Cisternas et al. (2011), Schramm et al. (2013) re-analyzed by Ding et al. (2020). The virial BH masses were estimated based on single-epoch spectra using broad Hβ and/or broad Mg II. The comparison sample includes 32 objects from Cisternas et al. (2011) and 16 objects from Schramm et al. (2013). The total stellar masses of the Cisternas et al. (2011) sample were estimated by the empirical relation between M_*/L and redshift and luminosity in the *HST F814W* band, which was established using a sample of 199 AGN host galaxies. The total stellar masses for the Schramm et al. (2013) sample were estimated from the galaxy absolute magnitude M_V and rest-frame $(B - V)$ colour measured from *HST* imaging for

[4]X-ray: Generate and Analyse GitHub

[5]*XMM* Exploration Jupyter Notebook

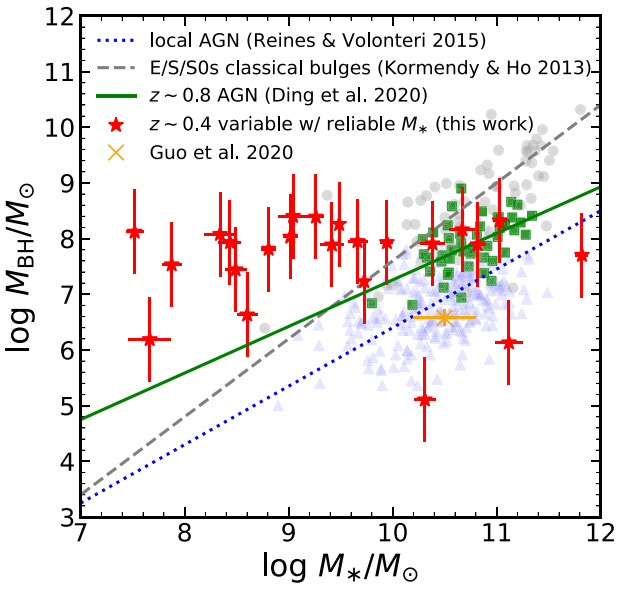

Figure 18. BH masses estimated from the damping time-scales using the relation of Burke et al. (2021) versus host galaxy stellar mass M_* estimates from SED fitting for our variable sources with constrained variability time-scales and reliable stellar mass estimates (red star symbols). For comparison, we show the scaling relations from X-ray selected intermediate-redshift AGNs and local samples of AGNs and inactive galaxies. The green solid line shows the best-fitting relation of the sample of 48 X-ray selected AGNs with a median $z \sim 0.8$ from Cisternas et al. (2011) and Schramm et al. (2013) re-analyzed by Ding et al. (2020), with individual sources shown as green square symbols. The blue dotted line represents the best-fit relation in local AGNs from Reines & Volonteri (2015), with individual sources shown as blue triangle symbols. The grey dashed line denotes the best-fitting relation using the sample of ellipticals and spiral/S0 galaxies with classical bulges from Kormendy & Ho (2013), with individual sources shown as grey circle symbols. The DES variability-selected dwarf AGN from Guo et al. (2020) is shown as the orange '×' symbol. The error bars on the red points are statistical uncertainties.

quasar-host decomposition using the M/L calibration of Bell et al. (2003).

Also shown for context in Fig. 18 are the best-fitting scaling relations for local samples of inactive galaxies (e.g. Häring & Rix 2004; Kormendy & Ho 2013; McConnell & Ma 2013) and low-redshift AGNs (Reines & Volonteri 2015). Our sample appears broadly consistent with the relation of Reines & Volonteri (2015) or the $z \sim 0.8$ AGNs. This is not unexpected given the typical redshfit of our sources of $z \sim 0.4$, in-between the intermediate-redshift and local AGN populations. However, any apparent offset is likely insignificant accounting for possible systematic uncertainties in the stellar mass estimates. Also, by imposing the cut on the variability time-scale, we introduce a selection effect which may reduce the correlation. While based on only 11 data points and the results of Guo et al. (2020), our results may suggest no significant redshift evolution in the M_{BH}–M_* scaling relation from redshift $z \sim 1$ to $z \sim 0$ (see also Ding et al. 2020; Li et al. 2021), which is consistent with previous results based on the M_{BH}–σ_* relation (e.g. Shen et al. 2015; Sexton et al. 2019).

5 CONCLUSIONS

We have identified 706 candidate AGNs at $z < 1.5$ in the DES deep fields using optical variability. Using SED fitting for stellar mass estimation, we found 26 candidate dwarf AGNs with host stellar mass $M_* < 10^{9.5}\,M_\odot$ (at a median photometric redshift of $\langle z \rangle \sim 0.9$) and 15 candidates with short-time-scale variability $\langle z \rangle \sim 0.4$. Our dwarf AGNs are at higher redshift at a given stellar mass than previous variability-selected dwarf AGN samples, and on-par with dwarf AGN identification in deep X-ray/radio surveys. Such dwarf AGNs at these intermediate redshifts are more likely to be pristine analogues of SMBH seeds that formed at high redshift. We measure the variable AGN fraction in our parent galaxy sample of 63 721 objects, which, consistent with previous work, depends on stellar mass due to a variety of selection effects (Burke et al. 2022). However, we caution that our sample is likely to contain some false positives given the AGN/star formation degeneracies in stellar mass estimates and scatter in the BH – host galaxy stellar mass relation. Our candidates require further follow-up to measure their BH masses.

Analysis of the X-ray and MIR fluxes in most of our variable sources is consistent with their AGN nature. However, their host stellar mass estimates remain somewhat uncertain given the limitations of optical and NIR SED fitting and contamination from the AGN emission. Nevertheless, our catalogue of variable intermediate-redshift dwarf AGNs with high-quality optical light curves in legacy fields probes a unique parameter space of dwarf AGN searches. Extension to deep field public catalogues with uniformly extracted photometry from the UV to MIR (e.g. Davies et al. 2021) will help constrain the stellar mass estimates. Future deep-imaging surveys in the IR and UV will also help constrain the stellar masses at higher redshifts. High photometric precision and higher cadence light curves will enable detection and mass estimation of IMBHs using the relation of Burke et al. (2021). Continued monitoring in these deep fields is ongoing with DECam to further extend the light-curve duration, which will enable more robust measurements of the long-term AGN optical variability damping time-scale (Kozłowski 2021) for more accurate BH mass estimation. Surveys with a more rapid cadence will enable smaller variability time-scale measurements and probe even lower BH masses (Bellm et al. 2022). These data will be essential for enabling an accurate determination of the AGN occupation fraction in low-mass galaxies in the era of the Rubin Observatory (Ivezić et al. 2019).

ACKNOWLEDGEMENTS

CJB and Y-CC acknowledge support from the Illinois Graduate Survey Science Fellowship. XL, YS, and Y-CC acknowledge support by NSF grant AST-2108162. YS acknowledges support by NSF grant AST-2009947. This research was supported in part by the National Science Foundation under PHY-1748958.

We thank Brian Yanny and Ken Herner for help with the DES computing resources used for this work. We thank Richard Kessler for help obtaining the original DES-SN program light curves and for comments which improved the clarity of the text.

Funding for the DES Projects has been provided by the U.S. Department of Energy, the U.S. National Science Foundation, the Ministry of Science and Education of Spain, the Science and Technology Facilities Council of the United Kingdom, the Higher Education Funding Council for England, the National Center for Supercomputing Applications at the University of Illinois at Urbana-Champaign, the Kavli Institute of Cosmological Physics at the University of Chicago, the Center for Cosmology and Astro-Particle Physics at the Ohio State University, the Mitchell Institute for Fundamental Physics and Astronomy at Texas A&M University, Financiadora de Estudos e Projetos, Fundação Carlos Chagas Filho de Amparo à Pesquisa do Estado do Rio de Janeiro, Conselho Nacional de Desenvolvimento

Científico e Tecnológico and the Ministério da Ciência, Tecnologia e Inovação, the Deutsche Forschungsgemeinschaft and the Collaborating Institutions in the Dark Energy Survey.

The Collaborating Institutions are Argonne National Laboratory, the University of California at Santa Cruz, the University of Cambridge, Centro de Investigaciones Energéticas, Medioambientales y Tecnológicas-Madrid, the University of Chicago, University College London, the DES-Brazil Consortium, the University of Edinburgh, the Eidgenössische Technische Hochschule (ETH) Zürich, Fermi National Accelerator Laboratory, the University of Illinois at Urbana-Champaign, the Institut de Ciències de l'Espai (IEEC/CSIC), the Institut de Física d'Altes Energies, Lawrence Berkeley National Laboratory, the Ludwig-Maximilians Universität München and the associated Excellence Cluster Universe, the University of Michigan, the National Optical Astronomy Observatory, the University of Nottingham, The Ohio State University, the University of Pennsylvania, the University of Portsmouth, SLAC National Accelerator Laboratory, Stanford University, the University of Sussex, Texas A&M University, and the OzDES Membership Consortium.

Based in part on observations at Cerro Tololo Inter-American Observatory, National Optical Astronomy Observatory, which is operated by the Association of Universities for Research in Astronomy (AURA) under a cooperative agreement with the National Science Foundation.

The DES data management system is supported by the National Science Foundation under Grant Numbers AST-1138766 and AST-1536171. The DES participants from Spanish institutions are partially supported by MINECO under grants AYA2015-71825, ESP2015-66861, FPA2015-68048, SEV-2016-0588, SEV-2016-0597, and MDM-2015-0509, some of which include ERDF funds from the European Union. IFAE is partially funded by the CERCA program of the Generalitat de Catalunya. Research leading to these results has received funding from the European Research Council under the European Union's Seventh Framework Program (FP7/2007-2013) including ERC grant agreements 240672, 291329, and 306478. We acknowledge support from the Brazilian Instituto Nacional de Ciência e Tecnologia (INCT) e-Universe (CNPq grant 465376/2014-2).

This manuscript has been authored by Fermi Research Alliance, LLC under Contract No. DE-AC02-07CH11359 with the U.S. Department of Energy, Office of Science, Office of High Energy Physics.

DATA AVAILABILITY

The deep field photomtery catalogue will be made available as part of the cosmology data products release, following the completion of the DES 3-yr weak-lensing and galaxy-clustering cosmology work. When available, optical spectra can be found following the references in Hartley et al. (2022). Supplementary catalogues (e.g. *WISE*, *Chandra*, ZFOURGE) are available following the references provided in the text.

REFERENCES

Agostino C. J., Salim S., 2019, ApJ, 876, 12
Alard C., 2000, A&AS, 144, 363
Alard C., Lupton R. H., 1998, ApJ, 503, 325
Angus C. R. et al., 2019, MNRAS, 487, 2215
Assef R. J. et al., 2013, ApJ, 772, 26
Bañados E. et al., 2018, Nature, 553, 473
Baldassare V. F., Reines A. E., Gallo E., Greene J. E., 2015, ApJ, 809, L14
Baldassare V. F. et al., 2016, ApJ, 829, 57
Baldassare V. F., Geha M., Greene J., 2018, ApJ, 868, 152
Baldassare V. F., Geha M., Greene J., 2020, ApJ, 896, 10
Baldwin J. A., Phillips M. M., Terlevich R., 1981, Publ. Astron. Soc. Pac., 93, 5
Barth A. J., Ho L. C., Rutledge R. E., Sargent W. L. W., 2004, ApJ, 607, 90
Becker A. C., 2017, Astrophysics Source Code Library, record ascl:1504.004
Begelman M. C., Volonteri M., Rees M. J., 2006, MNRAS, 370, 289
Bell E. F., McIntosh D. H., Katz N., Weinberg M. D., 2003, ApJS, 149, 289
Bellm E. C., Burke C. J., Coughlin M. W., Andreoni I., Raiteri C. M., Bonito R., 2022, ApJS, 258, 13
Bellovary J. M., Cleary C. E., Munshi F., Tremmel M., Christensen C. R., Brooks A., Quinn T. R., 2019, MNRAS, 482, 2913
Bernstein G. M. et al., 2017, Publ. Astron. Soc. Pac., 129, 114502
Bertin E., Arnouts S., 1996, A&AS, 117, 393
Blecha L. et al., 2016, MNRAS, 456, 961
Boquien M., Burgarella D., Roehlly Y., Buat V., Ciesla L., Corre D., Inoue A. K., Salas H., 2019, A&A, 622, A103
Bromm V., Loeb A., 2003, ApJ, 596, 34
Bruzual G., Charlot S., 2003, MNRAS, 344, 1000
Burgarella D., Buat V., Iglesias-Páramo J., 2005, MNRAS, 360, 1413
Burke C. J. et al., 2020, ApJ, 894, L5
Burke C. J. et al., 2021, Science, 373, 789
Burke C. J., Shen Y., Liu X., Natarajan P., Caplar N., Bellovary J. M., Wang Z. F., 2022, preprint (arXiv:2207.04092)
Butler N. R., Bloom J. S., 2011, AJ, 141, 93
Calzetti D., Armus L., Bohlin R. C., Kinney A. L., Koornneef J., Storchi-Bergmann T., 2000, ApJ, 533, 682
Cann J. M., Satyapal S., Abel N. P., Blecha L., Mushotzky R. F., Reynolds C. S., Secrest N. J., 2019, ApJ, 870, L2
Cann J. M. et al., 2021, ApJ, 912, L2
Cartier R. et al., 2015, ApJ, 810, 164
Chabrier G., 2003, Publ. Astron. Soc. Pac., 115, 763
Ciesla L. et al., 2015, A&A, 576, A10
Cisternas M. et al., 2011, ApJ, 741, L11
Civano F. et al., 2012, ApJS, 201, 30
Dark Energy Survey Collaboration, 2016, MNRAS, 460, 1270
Davies L. J. M. et al., 2021, MNRAS, 506, 256
De Cicco D. et al., 2015, A&A, 574, A112
De Cicco D. et al., 2019, A&A, 627, A33
Della Costa J. I., Sarajedini V. L., Strolger L.-G., 2020, ApJ, 894, 56
Desai S. et al., 2012, ApJ, 757, 83
Ding X. et al., 2020, ApJ, 888, 37
Draine B. T. et al., 2007, ApJ, 663, 866
Draine B. T. et al., 2014, ApJ, 780, 172
Elmer E., Almaini O., Merrifield M., Hartley W. G., Maltby D. T., Lawrence A., Botti I., Hirst P., 2020, MNRAS, 493, 3026
Evans I. N. et al., 2010, ApJS, 189, 37
Fan X. et al., 2001, AJ, 122, 2833
Filippenko A. V., Ho L. C., 2003, ApJ, 588, L13
Fiore F. et al., 2012, A&A, 537, A16
Flaugher B. et al., 2015, AJ, 150, 150
Foreman-Mackey D., Hogg D. W., Lang D., Goodman J., 2013, Publ. Astron. Soc. Pac., 125, 306
Foreman-Mackey D., Agol E., Ambikasaran S., Angus R., 2017, AJ, 154, 220
Garcet O. et al., 2007, A&A, 474, 473
Greene J. E., 2012, Nat. Commun., 3, 1304
Greene J. E., Strader J., Ho L. C., 2020, ARA&A, 58, 257
Groves B. A., Heckman T. M., Kauffmann G., 2006, MNRAS, 371, 1559
Guo H., Shen Y., Wang S., 2018, Astrophysics Source Code Library, record ascl:1809.008
Guo H. et al., 2020, MNRAS, 496, 3636
Gürkan M. A., Freitag M., Rasio F. A., 2004, ApJ, 604, 632
Haehnelt M. G., Rees M. J., 1993, MNRAS, 263, 168
Häring N., Rix H.-W., 2004, ApJ, 604, L89

Hartley W. G. et al., 2022, MNRAS, 509, 3547
Inayoshi K., Visbal E., Haiman Z., 2020, ARA&A, 58, 27
Inoue A. K., 2011, MNRAS, 415, 2920
Ivezić Ž. et al., 2019, ApJ, 873, 111
Jarvis M. J. et al., 2013, MNRAS, 428, 1281
Kelly B. C., Bechtold J., Siemiginowska A., 2009, ApJ, 698, 895
Kelly B. C., Sobolewska M., Siemiginowska A., 2011, ApJ, 730, 52
Kessler R. et al., 2015, AJ, 150, 172
Kimura Y., Yamada T., Kokubo M., Yasuda N., Morokuma T., Nagao T., Matsuoka Y., 2020, ApJ, 894, 24
Kirby E. N., Cohen J. G., Guhathakurta P., Cheng L., Bullock J. S., Gallazzi A., 2013, ApJ, 779, 102
Kormendy J., Ho L. C., 2013, ARA&A, 51, 511
Kormendy J., Richstone D., 1995, ARA&A, 33, 581
Kozłowski S., 2017, ApJS, 228, 9
Kozłowski S., 2021, AcA, 71, 103
Kumar S. et al., 2015, ApJ, 802, 27
LIGO Scientific Collaboration, Virgo Collaboration, 2020, Phys. Rev. Lett., 125, 101102
Leauthaud A. et al., 2007, ApJS, 172, 219
Leitherer C., Li I. H., Calzetti D., Heckman T. M., 2002, ApJS, 140, 303
Li J. I. H. et al., 2021, ApJ, 906, 103
Lidman C. et al., 2020, MNRAS, 496, 19
Ljung G. M., Box G. E. P., 1978, Biometrika, 65, 297
Luo B. et al., 2017, ApJS, 228, 2
McConnell N. J., Ma C.-P., 2013, ApJ, 764, 184
McCracken H. J. et al., 2012, A&A, 544, A156
MacLeod C. L. et al., 2010, ApJ, 721, 1014
Maccacaro T., Gioia I. M., Wolter A., Zamorani G., Stocke J. T., 1988, ApJ, 326, 680
Madau P., Rees M. J., 2001, ApJ, 551, L27
Martínez-Palomera J., Lira P., Bhalla-Ladd I., Förster F., Plotkin R. M., 2020, ApJ, 889, 113
Mejía-Restrepo J. E., Trakhtenbrot B., Lira P., Netzer H., Capellupo D. M., 2016, MNRAS, 460, 187
Mezcua M., Domínguez Sánchez H., 2020, ApJ, 898, L30
Mezcua M., Civano F., Marchesi S., Suh H., Fabbiano G., Volonteri M., 2018, MNRAS, 478, 2576
Mezcua M., Suh H., Civano F., 2019, MNRAS, 488, 685
Molina M., Reines A. E., Latimer C. J., Baldassare V., Salehirad S., 2021, ApJ, 922, 155
Mountrichas G., Buat V., Georgantopoulos I., Yang G., Masoura V. A., Boquien M., Burgarella D., 2021, A&A, 653, A70
Noll S., Burgarella D., Giovannoli E., Buat V., Marcillac D., Muñoz-Mateos J. C., 2009, A&A, 507, 1793
Oke J. B., Gunn J. E., 1983, ApJ, 266, 713
Oliver S. et al., 2000, MNRAS, 316, 749
Palmese A., Conselice C. J., 2021, Phys. Rev. Lett., 126, 181103
Portegies Zwart S. F., Baumgardt H., Hut P., Makino J., McMillan S. L. W., 2004, Nature, 428, 724
Poulain M. et al., 2020, A&A, 634, A50
Pouliasis E. et al., 2019, MNRAS, 487, 4285
Ramos Padilla A. F., Wang L., Małek K., Efstathiou A., Yang G., 2022, MNRAS, 510, 687
Reines A. E., Comastri A., 2016, Publ. Astron. Soc. Aust., 33, e054
Reines A. E., Volonteri M., 2015, ApJ, 813, 82
Reines A. E., Greene J. E., Geha M., 2013, ApJ, 775, 116
Reines A. E., Condon J. J., Darling J., Greene J. E., 2020, ApJ, 888, 36
Rest A. et al., 2014, ApJ, 795, 44
Ricarte A., Natarajan P., 2018, MNRAS, 481, 3278
Romer A. K., Viana P. T. P., Liddle A. R., Mann R. G., 2001, ApJ, 547, 594
Rumbaugh N. et al., 2018, ApJ, 854, 160
Sánchez-Sáez P., Lira P., Mejía-Restrepo J., Ho L. C., Arévalo P., Kim M., Cartier R., Coppi P., 2018, ApJ, 864, 87
Schlafly E. F., Meisner A. M., Green G. M., 2019, ApJS, 240, 30
Schramm M. et al., 2013, ApJ, 773, 150
Secrest N. J., Satyapal S., 2020, ApJ, 900, 56
Sesar B. et al., 2007, AJ, 134, 2236
Sexton R. O., Canalizo G., Hiner K. D., Komossa S., Woo J.-H., Treister E., Hiner Dimassimo S. L., 2019, ApJ, 878, 101
Shen Y., 2013, Bull. Astron. Soc. India, 41, 61
Shen Y. et al., 2015, ApJ, 805, 96
Shen Y. et al., 2019, ApJS, 241, 34
Soumagnac M. T. et al., 2015, MNRAS, 450, 666
Stalevski M., Fritz J., Baes M., Nakos T., Popović L. Č., 2012, MNRAS, 420, 2756
Stalevski M., Ricci C., Ueda Y., Lira P., Fritz J., Baes M., 2016, MNRAS, 458, 2288
Stern D. et al., 2012, ApJ, 753, 30
Straatman C. M. S. et al., 2016, ApJ, 830, 51
Suberlak K. L., Ivezić Ž., MacLeod C., 2021, ApJ, 907, 96
Tie S. S. et al., 2017, AJ, 153, 107
Tomczak A. R. et al., 2014, ApJ, 783, 85
Trevese D., Boutsia K., Vagnetti F., Cappellaro E., Puccetti S., 2008, A&A, 488, 73
Trump J. R. et al., 2015, ApJ, 811, 26
Turner D. J., Giles P. A., Romer A. K., Korbina V., 2022, preprint (arXiv:2202.01236)
Veilleux S., Osterbrock D. E., 1987, ApJS, 63, 295
Volonteri M., 2010, A&A Rev., 18, 279
Wang F. et al., 2021, ApJ, 907, L1
Ward C. et al., 2021a, preprint (arXiv:2110.13098)
Ward C. et al., 2021b, ApJ, 913, 102
Webb N. A. et al., 2020, A&A, 641, A136
Weisz D. R., Dolphin A. E., Skillman E. D., Holtzman J., Gilbert K. M., Dalcanton J. J., Williams B. F., 2014, ApJ, 789, 147
Wu X.-B. et al., 2015, Nature, 518, 512
Xue Y. Q., 2017, New Astron Rev., 79, 59
Yan R., Blanton M. R., 2012, ApJ, 747, 61
Yang Q. et al., 2017, AJ, 154, 269
Yang G. et al., 2022, ApJ, 927, 192
Young M. et al., 2012, ApJ, 748, 124
Zou F. et al., 2022, ApJSS, 262, 15

SUPPORTING INFORMATION

Supplementary data are available at *MNRAS* online.

table2.tex

Please note: Oxford University Press is not responsible for the content or functionality of any supporting materials supplied by the authors. Any queries (other than missing material) should be directed to the corresponding author for the article.

APPENDIX A: PHOTOMETRIC ERROR CORRECTION

The uncertainties on the photometry derived from SExtractor do not include systematic sources of error, particularly relevant for fainter sources. To correct for systematic scatter in the photometry, we follow the method of Sesar et al. (2007). We plot the RMS scatter of each light curve $\Sigma(m)$ as a function of median magnitude for each light curve using all sources in each field. Therefore, it is a good assumption that most sources are not intrinsically variable. We then compute the median of $\Sigma(m)$ in bins of width 0.5 magnitudes and fit a fourth-order polynomial through the binned medians with errors given by RMS of $\Sigma(m)$ in each bin. Assuming most sources are not intrinsically variable, the corrected errors on each measurement are given by

$$\sigma_i' = \sqrt{\sigma_i^2 + \xi(m)^2}, \tag{A1}$$

where σ_i is the uncorrected error measurement and $\xi(m)$ is the fitted fourth-order polynomial evaluated at magnitude m. We perform this

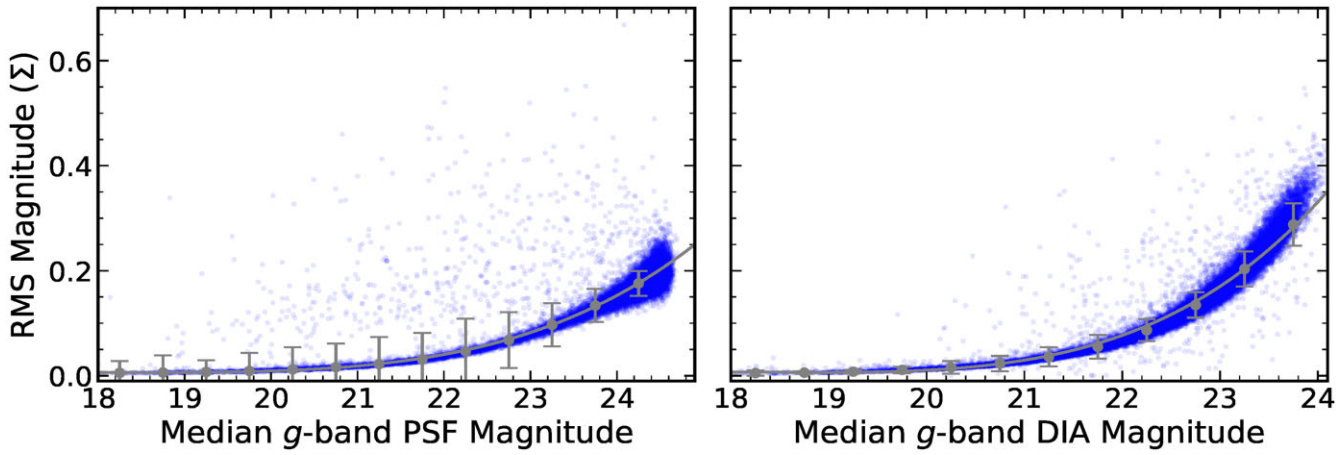

Figure A1. RMS magnitude Σ versus median *g*-band aperture magnitude for PSF (Panel a) and DIA (Panel b) SN-C3 light curves. The binned median and polynomial fit are shown in grey. The error bars are computed from the RMS of Σ in each bin.

correction separately for both PSF and DIA light curves. In general, DES has exceptionally stable photometry for sources brighter than $g \sim 20$ but the RMS scatter increases as expected for fainter sources. We show the scatter versus magnitude in the SN-C3 field in Fig. A1. The scatter is larger in DIA light curves because of the various artefacts and systematic sources of noise introduced with difference imaging.

APPENDIX B: DIFFERENCE IMAGING ZERO POINT SOLUTION

To determine the zero-point of our DIA magnitudes and to place our DIA photometry on the DES photometric system, we note that the DIA magnitudes with a 5-arcsec aperture should be equivalent to PSF magnitudes for unresolved sources. Therefore, in each field, we simply plot the median PSF versus DIA magnitudes for each unresolved source and perform linear regression. We take difference between the $y = x$ line and the fitted line and at $g = 20$ as the DIA zero-point solution. We show the result for SN-C3 sources in Fig. B1

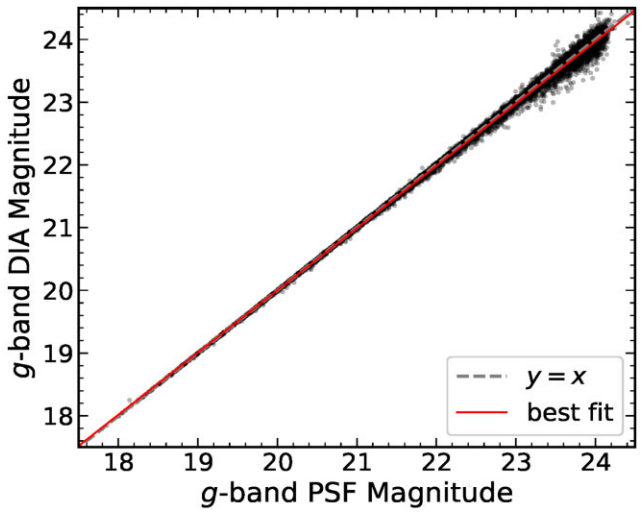

Figure B1. PSF versus DIA magnitudes for unresolved SN-C3 sources after correcting for the zero-point difference following the procedure described in Appendix B. The resulting linear regression and line of $y = x$ are shown after correction for comparison.

after performing the zero-point correction. The DIA magnitudes are tightly correlated with the PSF magnitudes, providing further validation of our difference imaging pipeline.

APPENDIX C: STELLAR MASS ESTIMATE VALIDATION

To validate our CIGALE stellar mass estimates described in Section 2.7, we compare our CIGALE stellar masses to ZFOURGE (Tomczak et al. 2014; Straatman et al. 2016). ZFOURGE is a deep medium-band imaging survey which provides an observational benchmark of galaxy properties at intermediate redshift. After matching our SN-C3 sources to ZFOURGE-CDFS sources, we compare the ZFOURGE results to our stellar masses from CIGALE and photometric redshifts from the Yang et al. (2017) method in Fig. C1. We find that our CIGALE stellar mass and redshifts are well-correlated with ZFOURGE. We find a root mean square error (RMSE) of 1.25 dex for non-variable galaxies. For the photometric redshift comparison, we compute RMSE(Δz), where $\Delta z = |z_{\rm ph} - z_{\rm ZFOURGE}|/(1 + z_{\rm ZFOURGE})$. We note that ZFOURGE does not consider an AGN component in their SED model, so the photometric redshift and stellar mass comparison of galaxies with luminous AGNs should be treated with caution.

This RMSE is consistent with previous findings that stellar mass estimates can include systematic scatter of up to 20 per cent due to differences in model assumptions, even when the photometric redshift is accurate (Ciesla et al. 2015; Boquien et al. 2019). In particular, we caution that star formation is often degenerate with UV/optical AGN emission from the accretion disc. We attempt to break this degeneracy by using variability information as a simple prior on the inclination angle of the standard SKIRTOR model AGN in CIGALE (variable/Type-I: $i < 30^{\rm o}$; non-variable/Type-II: $i > 30^{\rm o}$) but allow the AGN luminosity fraction to vary between 0.1 and 0.9 in either case.

Finally, we use the available spectroscopic redshifts of our deep field DES sources from Hartley et al. (2022) (see their table 5) to benchmark our photometric redshifts (Figure C2). For the photometric redshift comparison, we compute RMSE(Δz), where $\Delta z = |z_{\rm ph} - z_{\rm sp}|/(1 + z_{\rm sp})$. Here, $z_{\rm ph}$ denotes our photometric redshift estimate and $z_{\rm sp}$ denotes the spectroscopic redshift. We find an RMSE of 0.25 for the non-variable galaxies and 0.35 for variable galaxies. The

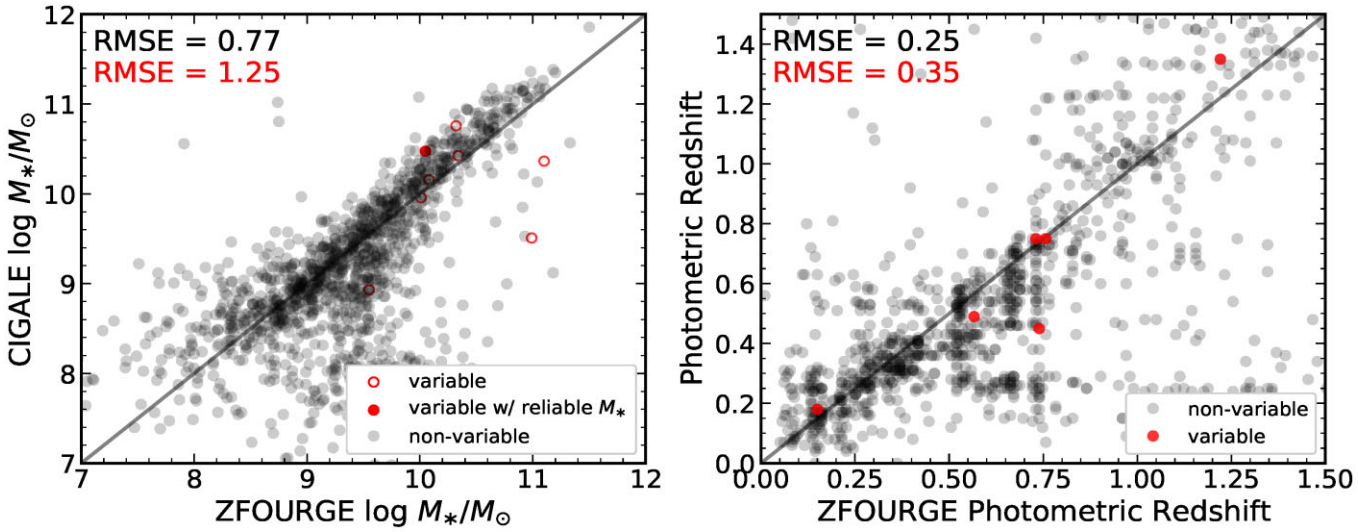

Figure C1. Stellar mass and photometric redshift comparison between our results and ZFOURGE. The RMSE for the variable (red) and non-variable (black) sources are shown in the upper left-hand corner of each panel.

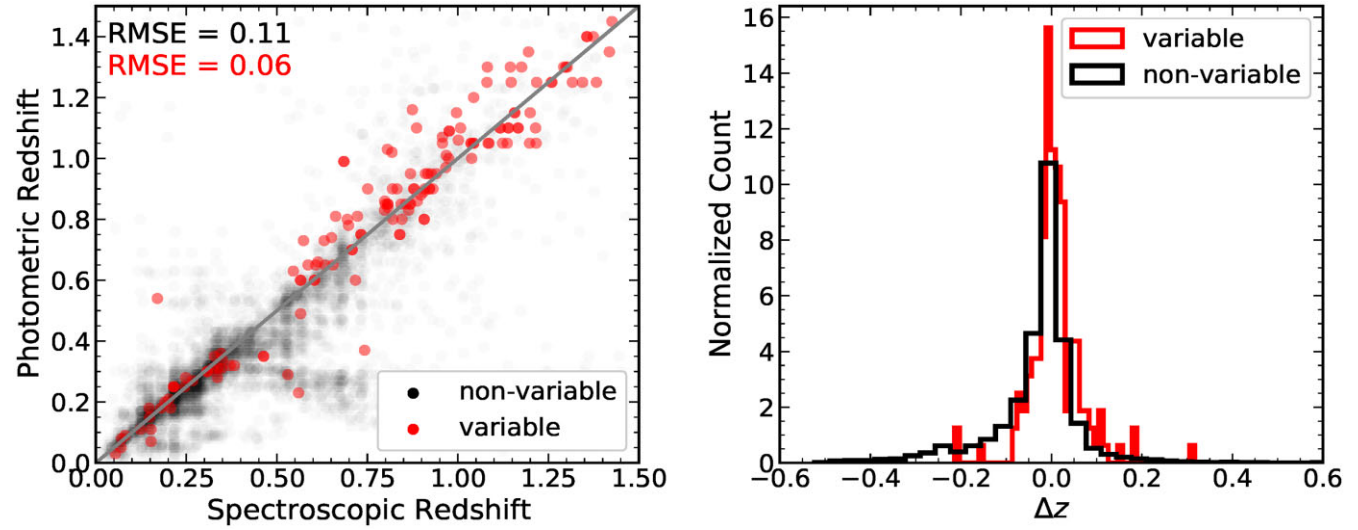

Figure C2. Photometric redshifts versus matched sources with secure spectroscopic redshifts. The RMSE for the variable (red) and non-variable (black) sources are shown in the upper left-hand corner of the figure.

details of the photometric redshift technique are given in Yang et al. (2017).

[1]*Department of Astronomy, University of Illinois at Urbana-Champaign, 1002 West Green Street, Urbana, IL 61801, USA*
[2]*Center for AstroPhysical Surveys, National Center for Supercomputing Applications, 1205 West Clark Street, Urbana, IL 61801, USA*
[3]*National Center for Supercomputing Applications, 1205 West Clark Street, Urbana, IL 61801, USA*
[4]*Department of Astronomy, University of Geneva, ch. d'Ecogia 16, CH-1290 Versoix, Switzerland*
[5]*Jodrell Bank Centre for Astrophysics, School of Physics & Astronomy, The University of Manchester, Manchester M13 9PL, UK*
[6]*Fermi National Accelerator Laboratory, P.O. Box 500, Batavia, IL 60510, USA*
[7]*Kavli Institute for Cosmological Physics, University of Chicago, Chicago, IL 60637, USA*
[8]*Department of Physics and Astronomy, 4129 Frederick Reines Hall, University of California, Irvine, CA 92697-4575, USA*
[9]*Department of Physics, University of Illinois at Urbana-Champaign, 1110 West Green Street, Urbana, IL 61801, USA*
[10]*Department of Astronomy & Astrophysics, The University of Chicago, Chicago, IL 60637, USA*
[11]*Department of Physics and Astronomy, Pevensey Building, University of Sussex, Brighton BN1 9QH, UK*
[12]*The Research School of Astronomy and Astrophysics, Australian National University, ACT 2601, Australia*
[13]*Center for Cosmology and Astro-Particle Physics, The Ohio State University, Columbus, OH 43210, USA*
[14]*Kavli Institute for Particle Astrophysics & Cosmology, P.O. Box 2450, Stanford University, Stanford, CA 94305, USA*
[15]*Brookhaven National Laboratory, Bldg 510, Upton, NY 11973, USA*
[16]*Laboratório Interinstitucional de e-Astronomia - LIneA, Rua Gal. José Cristino 77, Rio de Janeiro, RJ - 20921-400, Brazil*

[17]*Instituto de Física Teórica, Universidade Estadual Paulista, São Paulo, SP - 01140-070, Brazil*
[18]*Institute of Cosmology and Gravitation, University of Portsmouth, Portsmouth PO1 3FX, UK*
[19]*CNRS, UMR 7095, Institut d'Astrophysique de Paris, F-75014, Paris, France*
[20]*Sorbonne Universités, UPMC Univ Paris 06, UMR 7095, Institut d'Astrophysique de Paris, F-75014 Paris, France*
[21]*Department of Physics & Astronomy, University College London, Gower Street, London WC1E 6BT, UK*
[22]*Institut de Física d'Altes Energies (IFAE), The Barcelona Institute of Science and Technology, Campus UAB, E-08193 Bellaterra (Barcelona), Spain*
[23]*University of Nottingham, School of Physics and Astronomy, Nottingham NG7 2RD, UK*
[24]*Astronomy Unit, Department of Physics, University of Trieste, via Tiepolo 11, I-34131 Trieste, Italy*
[25]*INAF-Osservatorio Astronomico di Trieste, via G. B. Tiepolo 11, I-34143 Trieste, Italy*
[26]*Institute for Fundamental Physics of the Universe, Via Beirut 2, I-34014 Trieste, Italy*
[27]*Observatório Nacional, Rua Gal. José Cristino 77, Rio de Janeiro, RJ - 20921-400, Brazil*
[28]*Department of Physics, University of Michigan, Ann Arbor, MI 48109, USA*
[29]*Hamburger Sternwarte, Universität Hamburg, Gojenbergsweg 112, D-21029 Hamburg, Germany*
[30]*School of Mathematics and Physics, University of Queensland, Brisbane, QLD 4072, Australia*
[31]*Centro de Investigaciones Energéticas, Medioambientales y Tecnológicas (CIEMAT), E-28040 Madrid, Spain*
[32]*Department of Physics, IIT Hyderabad, Kandi 502285, India*
[33]*Santa Cruz Institute for Particle Physics, Santa Cruz, CA 95064, USA*
[34]*Institute of Theoretical Astrophysics, University of Oslo, P.O. Box 1029 Blindern, NO-0315 Oslo, Norway*
[35]*Instituto de Fisica Teorica UAM/CSIC, Universidad Autonoma de Madrid, E-28049 Madrid, Spain*
[36]*Institut d'Estudis Espacials de Catalunya (IEEC), E-08034 Barcelona, Spain*
[37]*Institute of Space Sciences (ICE, CSIC), Campus UAB, Carrer de Can Magrans, s/n, E-08193 Barcelona, Spain*
[38]*Faculty of Physics, Ludwig-Maximilians-Universität, Scheinerstr. 1, D-81679 Munich, Germany*
[39]*Department of Physics, The Ohio State University, Columbus, OH 43210, USA*
[40]*Center for Astrophysics | Harvard & Smithsonian, 60 Garden Street, Cambridge, MA 02138, USA*
[41]*Australian Astronomical Optics, Macquarie University, North Ryde, NSW 2113, Australia*
[42]*Lowell Observatory, 1400 Mars Hill Rd, Flagstaff, AZ 86001, USA*
[43]*George P. and Cynthia Woods Mitchell Institute for Fundamental Physics and Astronomy, and Department of Physics and Astronomy, Texas A&M University, College Station, TX 77843, USA*
[44]*Institució Catalana de Recerca i Estudis Avançats, E-08010 Barcelona, Spain*
[45]*Physics Department, University of Wisconsin-Madison, 1150 University Avenue Madison, 2320 Chamberlin Hall, Madison, WI 53706-1390, USA*
[46]*Institute of Astronomy, University of Cambridge, Madingley Road, Cambridge CB3 0HA, UK*
[47]*Department of Astrophysical Sciences, Princeton University, Peyton Hall, Princeton, NJ 08544, USA*
[48]*SLAC National Accelerator Laboratory, Menlo Park, CA 94025, USA*
[49]*School of Physics and Astronomy, University of Southampton, Southampton, SO17 1BJ, UK*
[50]*Computer Science and Mathematics Division, Oak Ridge National Laboratory, Oak Ridge, TN 37831,USA*
[51]*Department of Physics, Stanford University, 382 Via Pueblo Mall, Stanford, CA 94305, USA*
[52]*Kavli Institute for Particle Astrophysics & Cosmology, P.O. Box 2450, Stanford University, Stanford, CA 94305, USA*
[53]*Max Planck Institute for Extraterrestrial Physics, Giessenbachstrasse, D-85748 Garching, Germany*
[54]*Universitäts-Sternwarte, Fakultät für Physik, Ludwig-Maximilians Universität München, Scheinerstr. 1, D-81679 München, Germany*

This paper has been typeset from a TEX/LATEX file prepared by the author.